International Journal of Heat and Mass Transfer 218 (2024) 124728

Contents lists available at ScienceDirect

International Journal of Heat and Mass Transfer

journal homepage: www.elsevier.com/locate/ijhmt

Validation and analysis of a coupled fluid-ablation framework for modeling low-temperature ablator

Aleksander L. Zibitsker [a,1], Joel A. McQuaid [b,2], Christoph Brehm [b,2], Alexandre Martin [a,*,1]

[a] University of Kentucky, Lexington, KY, 40506, United States of America
[b] University of Maryland, College Park, MD, 20742, United States of America

ARTICLE INFO

Keywords:
Hypersonics
Ablation
Camphor
Coupled physics
Overset grid solver
Material response

ABSTRACT

Ablation of certain highly volatile materials, such as camphor, naphthalene, and dry ice, can be achieved at relatively mild hypersonic conditions in unheated wind tunnels. This provides a convenient way to test fundamental aspects of the ablation process, develop measurement techniques, and validate numerical simulations. In this study, we develop a coupled framework between hypersonic flow and material response solvers and validate the numerical approach against recent experiments conducted by the von Karman Institute of Fluid Dynamics. The flow environment is modeled with an overset near body - Cartesian solver developed within CHAMPS. The solver is equipped with capabilities for automatic mesh generation, adaptive mesh refinement (AMR), and an interpolation algorithm for exchanging boundary conditions with external solvers. The material domain is modeled with a network of one-dimensional rays, incorporating a heat conduction solver, several types of surface ablation models, and a coupled system of surface balance equations required for coupling with the flow solver. The material environment in the simulation aims to closely match the experimental design of the ablating sample, which included a thin layer of camphor applied on top of a copper holder. By taking into account the cooling effect introduced by the back structure, we were able to achieve close agreement with the experimental data for the stagnation point recession and the overall shape change of the geometry. The obtained results are also compared to uncoupled equilibrium-based and steady-state (coupled) solutions, highlighting the importance of the coupled approach for modeling ablation problems. In addition, we explore the effects of different transport properties on the ablation rate of the material, highlighting a strong dependence on the diffusivity of the ablating species. Finally, using the flexibility of the developed algorithm, we explore the effect of the iterative scheme and coupling frequency between the solvers on the accuracy of the solution and the overall duration of the simulation.

1. Introduction

Designing the shape and thickness of a Thermal Protection System (TPS) for hypersonic vehicles is a complex and lengthy process that involves multiple wind tunnel and arc-jet tests, numerical simulations, and potential flight experiments. Reliable numerical simulation tools can greatly reduce the time required for TPS design and help to account for a range of conditions experienced in flight. A commonly used material for TPS applications is carbon. At high heating rates, a carbon-based TPS experiences a range of thermo-chemical processes at the surface, such as oxidation, nitridation, and sublimation. Sublimation is the most efficient process among the three in absorbing energy from the flow, due to the endothermic reaction involved in the phase change of the material. However, sublimation is also the most violent process in terms of mass removal from the surface due to the exponential nature of the sublimation rate. Depending on the pressure, carbon begins to sublimate at temperatures exceeding 3000 K, which requires high enthalpy conditions in the experiment to activate this thermally driven process. An alternative method of studying the effect of sublimation on the material recession, shape change, and interaction with

* Corresponding author.
E-mail addresses: alex.zibitsker@uky.edu (A.L. Zibitsker), jamcq@umd.edu (J.A. McQuaid), cbrehm1@umd.edu (C. Brehm), alexandre.martin@uky.edu (A. Martin).
[1] Department of Mechanical and Aerospace Engineering, 151 Ralph G. Anderson Building.
[2] Department of Aerospace Engineering, 3179 Glenn L. Martin Hall Building.

https://doi.org/10.1016/j.ijheatmasstransfer.2023.124728
Received 29 March 2023; Received in revised form 22 August 2023; Accepted 19 September 2023
Available online 3 October 2023

the flow environment is to use low-temperature ablators, such as dry-ice [1], naphthalene and camphor [2,3]. These materials sublimate at relatively low-enthalpy conditions that can be easily achieved in blow-down hypersonic tunnels.

Camphor is a widely tested low-temperature ablator due to its wide range of sublimation conditions (triple point: $T_{\text{triple}} = 453.3$ K, $p_{\text{triple}} = 51.4$ kPa) and ease of handling. Early tests on camphor include studies of nose-tip shape change at an angle of attack by Baker [2] and Charwat [4], and investigations of transition phenomena and cross-hatching pattern formation on conical geometries by Stock [5] and others [6,7]. Recent advancements in supercomputers and coupling procedures between Direct Numerical Simulations (DNS) and ablative material codes have led to renewed interest in studying transition-induced ablating patterns on a camphor surface [8,9]. In another study, the potential of predicting the shape change of a carbon-based heat shield with a surrogate material such as camphor was recently explored by Rotondi et al. [10]. The study has shown that under certain conditions, there is a reasonable agreement between the pressure and recession profiles of a carbon-based heat shield at in-flight conditions and a camphor-based heat shield at low-enthalpy on-ground conditions. This outcome is making camphor or another surrogate, low-temperature ablator, an attractive option for prototyping heat shield shapes in low-enthalpy experiments and using relatively simple numerical tools.

For many years, modeling the ablative behavior of TPS materials was performed with one-dimensional (1D) solvers due to their relative numerical simplicity and computational efficiency. One of the most familiar 1D solvers for ablation problems is the FIAT code [11], developed at NASA Ames in the 1990s as a more numerically stable and versatile successor of the CMA code from the Aerotherm Corporation [12]. FIAT has been used in numerous TPS design and analysis activities since its development, where the most recent include analysis of Stardust, Mars Science Laboratory, and Orion missions [13–15]. Another recent 1D thermal response and ablation code was developed at the Sandia National Laboratories [16,17]. The code was based on a control volume finite-element method, a contracting grid scheme, and fully-implicit time integration. Later, based on the developed methodology, MOPAR - material response code with surface ablation and pyrolysis gas was developed by Martin and Boyd [18]. The code was applied to study non-Darcian behavior of pyrolysis gas in TPS materials and later was successfully coupled to the hypersonic aerothermodynamics code LeMANS, showing a capability of simulating a generic re-entry of the IRV-2 vehicle [19].

Simulation of the coupled interaction between the hypersonic flow and material domains is a challenging task due to the large time scale difference between the two problems. Typically, the fluid solver needs a much smaller time step to advance the solution in time compared to the material solver. Although it is computationally inefficient to advance the material solver at the fluid time step, advancing the coupled system in this manner potentially offers the most accurate solution. With this in mind, unified-type solvers utilize the integration of the entire system of equations for both the fluid and solid domains in order to achieve a seamless coupling between two problems [20,21]. On the other hand, coupling the two solvers in a segregated manner provides the advantage of setting each solver's time step independently. In that approach, the boundary conditions are explicitly exchanged at the interface, allowing to set each solver time step independently [22]. Taking coarser material time steps or performing multiple "uncoupled" material steps can significantly reduce the computational time of the simulation. However, numerical instabilities and a loss of accuracy of the material solution can occur [23]. Alternatively, an implicit coupling between the two solvers can be performed, as shown in the number of studies [23–25]. In the implicit approach, the flow boundary conditions are interpolated during the "uncoupled" material steps. This can be achieved through an iterative procedure where the flow solver obtains multiple converged solutions at two or more consecutive coupling junctions. The material solver is then rerun based on the interpolated boundary profiles and the flow solver is re-converged again. A variation of the implicit approach for strong coupling was suggested by Martin and Boyd [19], where during the re-convergence of the flow domain, the material solver is called at a predefined frequency to update the boundary condition and leads the coupled system to a stronger convergence.

In this work, we develop a one-dimensional material response solver, applicable to non-charring surface ablation problems and couple a network of the 1D solvers to the hypersonic flow solver CHAMPS NBS-Cart [26–30] to simulate multi-dimensional problems. The coupled framework is validated based on the recent experiments conducted at the Von-Karman Institute (VKI) [31,32], where a sub-scale Phoebus capsule geometry covered with a thin layer of camphor was exposed to Mach 6 flow at multiple total pressure conditions. The validation of the coupled approach is performed against the measured stagnation point recession and shape change of the geometry. The sensitivity of the solution is explored with different transport property models of the camphor gas, utilizing available literature data, a Lewis number approach, and numerically computed properties with quantum-chemical simulation. The material domain is modeled as a stack-up structure, consisting of the camphor layer and copper holder to account for the heat soak-back effect. Finally, the accuracy and total duration of the simulation are explored with respect to the iterative scheme and coupling frequency between the solvers.

The outline of this work is as follows. The paper begins by presenting the governing equations for the fluid and material domains, including a list of the transport and physical properties of the gas and solid environments. The coupling scheme between the solvers and the iterative solution of surface balance equations is then presented. The results section includes a verification study of the flow and material domains, a validation study of the coupled framework, and concludes with a sensitivity study concerning the camphor transport properties, ablation model, type of back wall boundary condition, and the effect of the coupling scheme on the accuracy and duration of the solution.

2. Flow solver framework

2.1. Governing equations

The low enthalpy conditions in the Phoebus capsule experiment permit the assumption of thermal equilibrium and a non-reactive mixture in the fluid domain, thus significantly simplifying the governing equations. Blowing of camphor gas into the boundary layer modifies the local transport properties of the mixture and makes it important to model the flow as a multi-species environment. To do this, the NBS-Cart solver makes use of the thermochemical non-equilibrium framework in CHAMPS for modeling the multi-component gas. Due to the relatively low peak temperature of the flow, no chemical reactions are assumed to take place and hence, the fluid is modeled as a 3-species gas given by N_2, O_2 and $C_{10}H_{16}O$ (camphor). The governing equations for a non-reactive, multi-component gas are given in Eqn. (1) as

$$\frac{\partial \boldsymbol{U}}{\partial \boldsymbol{P}} \frac{\partial \boldsymbol{P}}{\partial t} + \nabla \cdot \left(\boldsymbol{F} - \boldsymbol{F}_{\boldsymbol{d}} \right) = 0, \tag{1}$$

where $\boldsymbol{U}$ is the conservative state vector, $\boldsymbol{P}$ is the primitive state vector, $\boldsymbol{F}$ is the convective flux, and $\boldsymbol{F}_{\boldsymbol{d}}$ is the viscous flux. Eqn. (2) presents the primitive and conservative state vectors, such that ρ_s is the species density, ρ is the mixture density, $\boldsymbol{V} = (u, v, w)^T$ is the fluid velocity vector with its specified components in the Cartesian reference frame, and E is the total energy component per unit volume.

$$\boldsymbol{U} = \begin{Bmatrix} \rho_s \\ \rho u \\ \rho v \\ \rho w \\ E \end{Bmatrix} \quad \text{and} \quad \boldsymbol{P} = \begin{Bmatrix} \rho_s \\ u \\ v \\ w \\ T \end{Bmatrix}. \tag{2}$$

The convective and viscous fluxes for direction i are given in Eqn. (3) as

$$\boldsymbol{F}=\begin{Bmatrix}\rho_s\hat{u}\\ \rho u\hat{u}+p\delta_{1i}\\ \rho v\hat{u}+p\delta_{2i}\\ \rho w\hat{u}+p\delta_{3i}\\ (E+p)\hat{u}\end{Bmatrix}\quad\text{and}\quad\boldsymbol{F_v}=\begin{Bmatrix}-\boldsymbol{J_{s,i}}\\ \boldsymbol{\tau_{1i}}\\ \boldsymbol{\tau_{2i}}\\ \boldsymbol{\tau_{3i}}\\ \left(\kappa_{tr}+\kappa_v\right)\boldsymbol{\nabla T}-\sum_{s=1}^{ns}\boldsymbol{J}_s h_s+\boldsymbol{\tau}\cdot\boldsymbol{V}\end{Bmatrix},\tag{3}$$

where p is the mixture pressure, $\boldsymbol{\tau}$ is the viscous stress tensor, κ_{tr} is the fluid thermal conductivity for the translational/rotational mode, κ_v is the fluid thermal conductivity for the vibrational mode, $J_{s,i}$ is the species mass diffusion flux in direction i for species s, h_s is the species enthalpy and $\hat{u}$ is defined as the contravariant velocity [33]. The total energy contained by a multi-component fluid at a given state is defined as

$$E=\sum_s^{ns}\rho_s C_{v,tr,s}T+\sum_s^{ns}\rho_s e_{v,s}+\sum_s^{ns}\rho_s h_s^f+\frac{1}{2}\rho(u^2+v^2+w^2),\tag{4}$$

where the first term represents the contribution from the translational and rotational energy modes, the second term is the contribution from the vibrational energy mode, the third term comes from the heat of formation of species h_s^f, the final component is from the kinetic energy, and ns represents the number of species. The total vibrational energy contained by the fluid is defined next as

$$E_v=\sum_s^{ns}\rho_s e_{v,s},\tag{5}$$

where,

$$e_{v,s}=\begin{cases}\frac{R_u}{M_s}\frac{\theta_{v,s}}{\exp(\theta_{v,s}/T_v)-1)} & \text{for molecules, and}\\ 0 & \text{for atoms.}\end{cases}\tag{6}$$

The parameter $\theta_{v,s}$ is the species characteristic vibrational temperature (provided in Table 4), R_u is the universal gas constant, and M_s is the molecular weight of species s. Both N_2 and O_2 do see vibrational activation at sufficiently high temperatures, however, for the cases shown in this work, vibrational effects are expected to be minimal. Camphor has been assumed to have no vibrationally activated modes at these conditions. The fluid temperature is not high enough to see electronic or radiative effects influencing the flow field, and so these contributions have been neglected in this work. Modeling of the species mass diffusion is performed with Fick's first law, however, this formulation does not guarantee that the mass diffusion fluxes will sum to zero, resulting in accuracy issues. Due to that, the mass diffusion flux in this work is assumed to follow modified Fick's law as suggested by Sutton and Gnoffo [34]. To apply the modified law, first, the species mass diffusion flux is computed with the equation below

$$\boldsymbol{I_s}=-\rho D_s\boldsymbol{\nabla}Y_s,\tag{7}$$

where ρ is the bulk gas density, D_s is the species diffusion coefficient and $\boldsymbol{\nabla}Y_s$ is the gradient of the species mass fraction. Then, the correction is applied to ensure the mass fluxes sum to zero as

$$\boldsymbol{J_s}=\boldsymbol{I_s}-Y_s\sum_{r=1}^{ns}\boldsymbol{I_r},\tag{8}$$

where $\boldsymbol{J_s}$ and $\boldsymbol{I_s}$ both represent the species mass diffusion vectors. The species diffusion coefficients are approximated in this work with a single binary coefficient D, computed depending on the model described later in this section.

2.2. Transport properties

The transport properties of the gaseous species include viscosity, thermal conductivity, and diffusivity, and the models for each property will be presented here. The viscosity of the air species, N_2 and O_2 is computed using the Blottner curve fit, Ref. [35], as shown in Eqn. (9) with the coefficients A_s, B_s, and C_s presented in Table 5 in the Appendix.

$$\mu_s=0.1\exp\left[\left(A_s\ln(T)+B_s\right)\ln(T)+C_s\right],\tag{9}$$

The air species conductivity is then related to the species viscosity using Eucken's relations, Ref. [36], as shown in Eqns. (10) and (11)

$$\kappa_{tr,s}=\frac{5}{2}\mu_s C_{v_{t,s}}+\mu_s C_{v_{r,s}},\tag{10}$$

and

$$\kappa_{v,s}=\mu_s C_{v_{v,s}}.\tag{11}$$

The terms $C_{v_{t,s}}$, $C_{v_{r,s}}$, and $C_{v_{v,s}}$ are the specific heats at constant volume for the translational, rotational, and vibrational energy modes given by

$$C_{v_{t,s}}=\frac{3}{2}\frac{R_u}{M_s}$$

$$C_{v_{r,s}}=\begin{cases}\frac{R_u}{M_s} & \text{for molecules,}\\ 0 & \text{for atoms and electrons.}\end{cases}$$

$$C_{v_{v,s}}=\frac{\partial e_{v,s}}{\partial T_v}=\begin{cases}\sum_{i=1}^{m} g_{s,i}\frac{R_u}{M_s}\frac{(\theta_{v_{s,i}}/T_v)^2\exp(\theta_{v_{s,i}}/T_v)}{(\exp(\theta_{v_{s,i}}/T_v)-1)^2} & \text{for molecules,}\\ 0 & \text{for atoms and electrons,}\end{cases}\tag{12}$$

where m denotes the number of vibrationally-activated energy modes for a given species, and $g_{s,i}$ denotes the degeneracy of the i-th energy level of species s. The two air species N_2 and O_2 have only one vibrationally-activated energy mode, $m=1$, and a single level of degeneracy.

The conductivity and viscosity of the camphor species were modeled based on the models from two sources. The first model was obtained from the Yaws' Handbook, where the relevant chapters for the transport properties under consideration are given in Refs. [37–39]. The handbook was compiled from available literature data and in general, provides an extensive list of properties for organic and inorganic compounds. The properties of the compounds are provided in a convenient polynomial curve fit form with a specified valid temperature range. The second model was obtained based on a Quantum Chemical (QC) simulation of a camphor molecule, performed by Haskins [40]. The simulation provided thermodynamic and collision integral data and allowed computing the transport properties of the camphor species using Mutation++ library [41]. The input to the Mutation++ library included the thermodynamic data in NASA 7 format and collision integral data in the form of dipole polarizability and effective electrons participating in polarization, shown in Table 6 and 7 in the Appendix. Utilizing the Mutation++ library, the viscosity and thermal conductivity of the camphor species were computed for a range of temperature values and curve-fitted into a polynomial form, similar to the Yaws' model. The curve fits for the viscosity and thermal conductivity are provided in Eqns. (13) and (14)

$$\mu(T)=c_0+c_1T+c_2T^2+c_3T^3\tag{13}$$

and

$$\kappa(T)=c_0+c_1T+c_2T^2+c_3T^3,\tag{14}$$

where the coefficients for the two models, from Yaws and Haskins, can be found in Table 8 of the Appendix. A comparison of the two models' prediction of viscosity and thermal conductivity has been plotted in Fig. 1(a) and 1(b), respectively. The magnitude of the properties differs by around a factor of two, showing higher viscosity and conductivity predicted from the QC simulation. It is difficult to point at the specific reason for the large difference between the two models as it is unclear what method was used to obtain the properties of camphor in

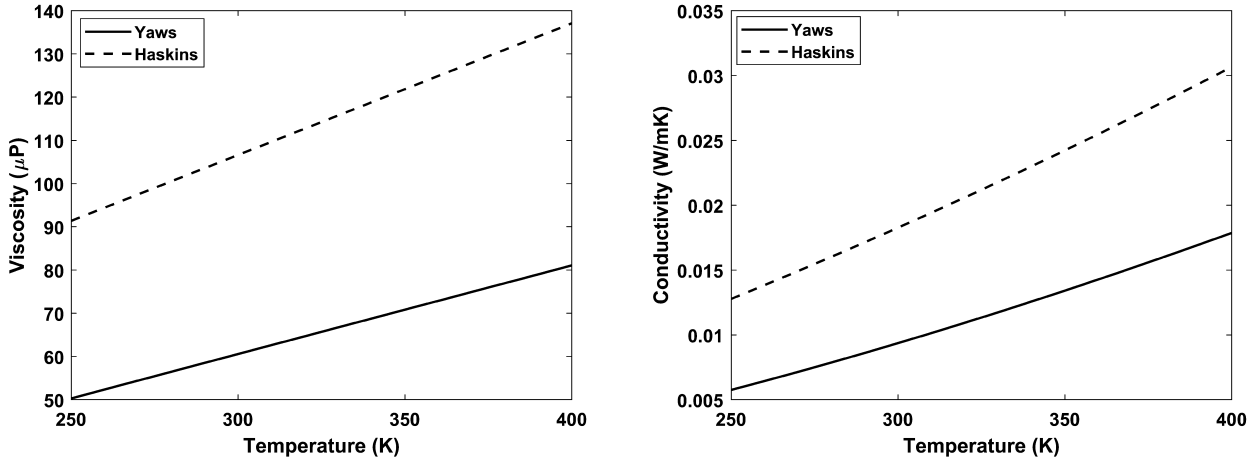

(a) Viscosity (b) Thermal conductivity

Fig. 1. Comparison of Yaws [37,38] and Haskins [40] viscosity and thermal conductivity models for camphor.

the Yaws handbook. However, as will be shown later in the results section, the given difference in the transport models is not proportional to the difference in the predicted surface quantities, and the factor of two differences between the models, leads to only a slight difference between the predicted results.

Given the individual viscosity and thermal conductivity of the air and camphor species, the mixture properties are computed in this work with Wilke's mixing rule as shown in Eqns. (15), (16)

$$\mu = \sum_{s}^{ns} \frac{X_s \mu_s}{\phi_s} \quad \text{and} \quad \kappa = \sum_{s}^{ns} \frac{X_s \kappa_s}{\phi_s}, \tag{15}$$

where X_s is the molar fraction of species s and ϕ_s is the mixing coefficient for species s given by

$$\phi_s = \sum_{r}^{ns} X_r \frac{\left[1 + \sqrt{\frac{\mu_s}{\mu_r}} \left(\frac{M_r}{M_s}\right)^{1/4}\right]^2}{\sqrt{8\left(1 + \frac{M_s}{M_r}\right)}}, \tag{16}$$

The last required transport property is the diffusion coefficient, which controls how effectively the near-wall species will diffuse away or toward the wall and thus, the sublimation rate of the material. In this work, three different models for a diffusion coefficient are tested to compare their relative effects. The first model uses a constant Lewis number approach, shown in the equation below

$$D = \frac{\mathrm{Le}\kappa_{\mathrm{tr}}}{\rho C_{p_{\mathrm{tr}}}}, \tag{17}$$

where Le is the Lewis number.[3] By assuming a Lewis number in the simulation and computing the local mixture density, conductivity, and specific heat, the effective diffusion coefficient of the mixture is derived.

In the second model, the binary coefficient for the diffusion of camphor in air is obtained from the Yaws' Handbook, chapter [39]. The coefficient is given as a function of temperature and is shown in a polynomial form below

$$D(T) = c_0 + c_1 T + c_2 T^2, \tag{18}$$

where the coefficients are provided in Table 9 in the Appendix.

Finally, in the third model, the diffusion coefficient of camphor is computed with the Mutation++ library based on the provided input from the QC simulation. The data was computed for a range of temperature and pressure values expected in the simulation and is plotted in Fig. 2(a), showing a strong dependence of the coefficient on the temperature at lower pressures. For convenience, the generated data was curve fitted with a polynomial product consisting of the temperature and pressure-dependent terms as shown in Eqn. (19) below. The coefficients of the polynomial were found with a least-squares method and are provided in Table 10 in the Appendix. Fig. 2(b) shows the comparison of the camphor diffusion coefficient computed with the Yaws' and Haskins' models. The Haskins' data was plotted at three pressures corresponding to the stagnation pressure predicted in the simulation. Comparatively, the diffusion coefficient from the Yaws model is lower than the one obtained from the QC simulation and the difference rapidly increases with decreasing pressure and mildly increases with increasing temperature.

$$D(T,p) = (B_1 T^2 + B_2 T + B_3)(B_4 p^{B_5}). \tag{19}$$

2.3. Thermal properties

The gaseous enthalpy of each individual species can be computed using the NASA 7 polynomials. The polynomial coefficients for the air species can be found in [42], while the coefficients for the camphor species were obtained based on the thermodynamic data computed in the QC simulation [40]. The coefficients in NASA 7 format for camphor species are given in Table 6 in the Appendix. The obtained gaseous enthalpy of camphor based on the QC simulation was verified against the reference study [32] and was found to closely agree with the data. With the known individual species enthalpies, the mixture enthalpy of the gas is computed in the following form

$$h = \sum_{k=1}^{ns} Y_k h_k \tag{20}$$

The properties of solid materials, such as camphor and copper used in the study are given in Table 12 in the Appendix. The properties of both materials are assumed to be constant based on the relatively small temperature increase of the materials.

2.4. NBS - cart solver

The flow environment is solved with an overset near body Cartesian solver developed within the CHAMPS framework. The solver was described in detail by McQuaid et al. [27] and is only briefly presented here. The solution starts by discretizing the entire domain with a block-structured Cartesian grid. The NBS grid is automatically generated from

[3] note that the Lewis number in the hypersonic community is assumed to be a ratio of thermal to mass diffusivity.

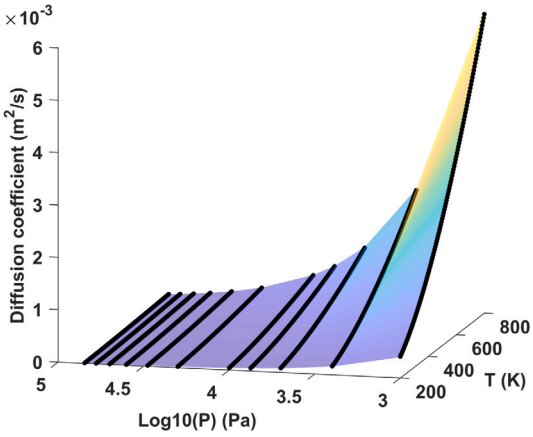

(a) QC simulation derived coefficient.

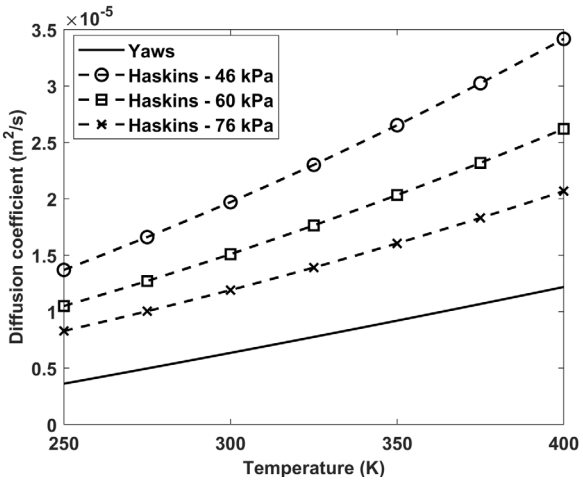

(b) Comparison of Yaws and QC derived diffusion coefficient at different pressures

Fig. 2. Diffusion coefficient of camphor in-air from a quantum-chemical (QC) simulation by Haskins [40] and polynomial curve fit by Yaws [39].

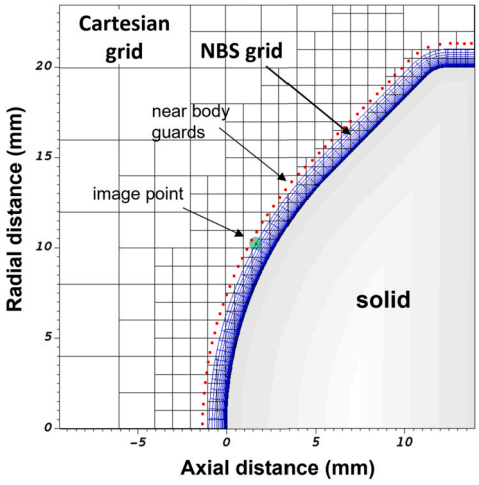

Fig. 3. Cartesian grid with Adaptive Mesh Refinement and near body Curvilinear grid overlaid on top. Note that each block on the Cartesian mesh contains $n_x \times n_y$ grid points. (For interpretation of the colors in the figure(s), the reader is referred to the web version of this article.)

a surface mesh, composed of any arbitrary set of elements, which is provided as an input at start-up. The surface nodes are used to project wall-normal node point distributions into the freestream to resolve the entire boundary layer. The Cartesian solver is set to resolve the off-body region and the AMR is used to track the shock structure during the surface recession. The NBS domain is solved in a sequential manner with the Cartesian grid solver, allowing the surface grid to be partitioned equally across all processors to maintain load balancing and scalability. A schematic of the mesh layout from the Phoebus capsule simulation is presented in Fig. 3. The gray grid denotes the off-body block-structured Cartesian mesh which remains relatively coarse all the way up to the geometry surface. Each Cartesian mesh block contains $n_x \times n_y$ points. The NBS grid is marked in blue and is a body-conformal stretched grid to resolve the near-wall gradients. The red dots in the figure denote the guard cells set by the NBS. Only a single layer of cells is shown, however, in practice, several layers are used to provide the means for higher-order accurate schemes. At the tip of each ray is an image point (midway between the guard cell and the last interior cell) which contains interpolated data from the Cartesian grid solution. The red guard cells can then be filled to impose the NBS inflow boundary condition. The NBS solution is coupled back onto the Cartesian near-wall cells via an overset interpolation algorithm, removing the need to treat any irregular points in the vicinity of the immersed surface.

The NBS solver uses a conservative finite difference numerical scheme on a generalized curvilinear grid to solve the full set of governing equations previously presented. The convective terms are computed using a 2nd-order MUSCL scheme with a modified Steger-warming flux scheme. The viscous fluxes are computed on the cell faces to maintain a 2nd order, conservative viscous treatment. The Cartesian grid solver employs a 5th-order WENO scheme [43] to accurately capture the off-body shock structure and uses a similar conservative viscous flux treatment as the NBS solver. The NBS resembles a structured grid layout in 2D which allows for the use of an efficient line-implicit Gauss-Seidel solver which may be used in both steady and unsteady flow simulations.

3. Material response solver framework

3.1. Governing equation and numerical model

The material thermal response with surface ablation is modeled with a one-dimensional transient heat conduction solver and a contracting grid scheme. The differential form of the one-dimensional transient material conduction with grid advection fluxes is shown in the equation below

$$\frac{dE_s}{dt} - \frac{d}{dx}\left(k_s \frac{dT}{dx} + E_s \omega\right) = 0, \tag{21}$$

where $E_s = \rho_s c_{p,s} T$ is the solid energy, ρ_s is the solid density, $c_{p,s}$ is the solid specific heat at constant pressure, k_s is the solid conductivity and ω is the grid face velocity.

The governing equation is discretized using an implicit finite-volume scheme with second-order accuracy in space and first-order accuracy in time. A schematic of a contracting one-dimensional mesh used for the discretization is shown in Fig. 4. The schematic includes two materials, the ablating part to the left and a back structure to the right. Two materials are assumed to be in perfect contact at the interface. In the scheme, only the left material is allowed to recess and the back structure maintains a constant length and a fixed size of the cells. The whole indices in the scheme represent cell centers and half indices represent face elements. The coordinate system is attached to the moving wall and points toward the end of the material. The residual length of the ablator is L^n and the current size of a cell is Δx_i. The amount of surface recession in the current step is Δs^n and the distance to the current and new location

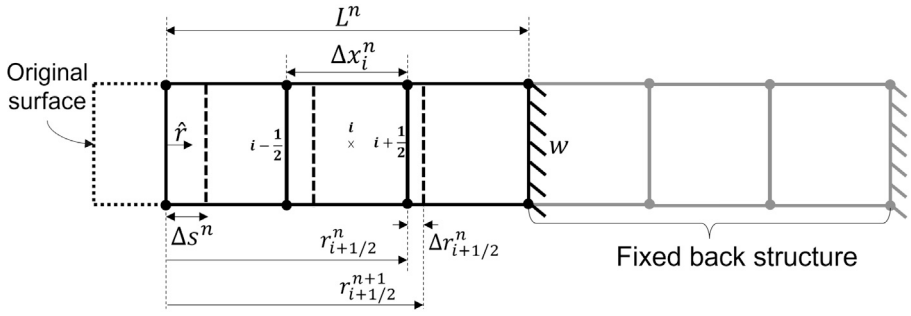

Fig. 4. Schematics of contracting one-dimensional mesh with back structure.

of the face is represented by $r_{i+1/2}^n$ and $r_{i+1/2}^{n+1}$ respectively. As a result, the incremental displacement of the given face element is $\Delta r_{i+1/2}^n$.

To simplify the discretization scheme, it is derived for materials with constant or quasi-constant properties, that do not vary "much" during the time and spatial integration. In the case of camphor and copper materials, that maintain constant properties, this assumption is applicable. The distribution of the cells is assumed non-uniform to better capture the near-wall gradients. The cross-sectional area of each cell is allowed to vary, depending on the type of element used: Cartesian, cylindrical or spherical. Following these assumptions, the compact form of the derived numerical scheme is given below

$$a_i T_i^{n+1} + a_{i-1} T_{i-1}^{n+1} + a_{i+1} T_{i+1}^{n+1} + b_i T_i^n = 0. \tag{22}$$

The linear coefficients of the discrete equation are written for the current time step as

$$\begin{aligned}
a_i &= \left[\frac{2\alpha_s A_{i+1/2}}{\Delta x_i + \Delta x_{i+1}} + \frac{2\alpha_s A_{i-1/2}}{\Delta x_{i-1} + \Delta x_i} \right. \\
&\quad \left. - \left(f_{i+1/2}\omega_{i+1/2} A_{i+1/2} - (1 - f_{i-1/2})\omega_{i-1/2} A_{i-1/2} \right) + \frac{1}{\Delta t} V_i \right], \\
a_{i-1} &= \left[-\frac{2\alpha_s A_{i-1/2}}{\Delta x_{i-1} + \Delta x_i} + f_{i-1/2}\omega_{i-1/2} A_{i-1/2} \right], \\
a_{i+1} &= \left[-\frac{2\alpha_s A_{i+1/2}}{\Delta x_i + \Delta x_{i+1}} - (1 - f_{i+1/2})\omega_{i+1/2} A_{i+1/2} \right] \\
\text{and} \quad b_i &= \left[-\frac{1}{\Delta t} V_i \right],
\end{aligned} \tag{23}$$

where $\alpha_s = \frac{k_s}{\rho_s c_{p,s}}$ is the thermal diffusivity, $A_{i+1/2}$ is the face area, V_i is the cell volume and $f_{i+1/2} = \frac{\Delta x_{i+1}}{\Delta x_i + \Delta x_{i+1}}$ represents a weighting coefficient in the piecewise linear profile of the heat conduction term. Variation in the area of the face elements in the discretized equation allows for the modeling of the material geometry in one of three coordinate systems, i.e. Cartesian, cylindrical, or spherical. The geometry dependence on the type of the coordinate systems is represented by the incremental area and volume elements in the grid as shown below

$$A_{i+1/2} = \frac{(2R_{i+1/2})^m \pi^{0.5m(3-m)}}{N} \quad \text{and} \quad V_i = \frac{\frac{2^m \pi^{0.5m(3-m)}}{m+1} \left(R_{i+1/2}^{m+1} - R_{i-1/2}^{m+1} \right)}{N}, \tag{24}$$

where $m = 0, 1$ or 2 represent a rectangular, cylindrical, or spherical geometry, $R_{i+1/2}$ is the distance to the face element from the base of the material stack-up and N is a parameter, representing spatial discretization of the modeled geometry in the case when the cylindrical or spherical surface is discretized with more than one element.

Displacement of the grid nodes due to surface recession is performed using a linear contraction scheme, where displacement of any given node is proportional to its distance from the back wall. With the known amount of surface recession Δs^n, the current ablator length L^n and the current location of the node $r_{i+1/2}^n$, the new location of the node is given as

$$r_{i+1/2}^{n+1} = r_w + r_{i+1/2}^n \left(1 - \frac{\Delta s^n}{L^n} \right), \tag{25}$$

where r_w is the location of the ablator back wall, as shown in Fig. 4. The grid face velocity in Eqn. (21) is then found from the incremental displacement of the face element with $\omega_{i+1/2} = (\Delta r_{i+1/2}^n)/\Delta t$. It should be noted, that this simple algorithm allows not only the contraction of the grid but also the expansion as a result of mass addition at the wall (negative Δs^n) due to possible condensation of the material. Once the linear system is constructed for each individual material ray, it forms a tridiagonal system of equations and is solved with Thomas algorithm [44].

4. Fluid-material coupling framework

4.1. Surface balance equations for finite-rate chemistry

To apply the boundary conditions for the fluid and material domains a set of surface balance equations for mass, momentum, and energy is solved at every interaction step between the solvers. The mass conservation at the wall represents a balance between the species flux reaching the wall by diffusion and chemical production versus the net species flux leaving the wall by advection and referred to as blowing. The mass balance equation is given below as

$$\underbrace{-\rho D_k \nabla Y_k}_{\text{diffusion}} + \underbrace{m_k''}_{\text{production}} = \underbrace{m_w'' Y_{k,w}}_{\text{blowing}}, \tag{26}$$

where m_k'' is the species chemical production flux and m_w'' is the net species blowing flux away from the wall. The mass balance equation is solved for the species mass fraction at the wall $Y_{k,w}$.

The net blowing flux away from the wall is computed by summing up the mass balance equation over all species at the wall. Assuming a binary diffusion coefficient of the species, the blowing flux is given by

$$m_w'' = (\rho u)_w = \sum_k^{ns} m_k'' = m_c'', \tag{27}$$

where the sum of production fluxes is equal to the ablation flux of camphor, m_c'', since no other species are produced at the wall. The net species flux away from the wall introduces a momentum exchange with the fluid cell and can be represented by the following momentum conservation at the wall, excluding the viscous fluxes

$$p_\eta = p_f + \rho_f u_f^2 = p_w + \rho_w u_w^2, \tag{28}$$

where the subscripts "w", "f" and "η" represent wall, flow and net conditions. The thermodynamic state of the gas can be computed with perfect gas law as given in the equation below

$$p = \rho R T, \tag{29}$$

where $R = R_u/\bar{M}$ and $\bar{M}$ is the mixture averaged molecular weight given by

$$\bar{M} = \frac{1}{\sum_k^{ns} \left(Y_k / M_k\right)}. \tag{30}$$

Combining Eqns. (27), (28) and (29) leads to expressions for the bulk gas velocity, pressure, and density at the wall

$$u_w = \frac{2RT_w m''_w}{p_\eta + \sqrt{p_\eta^2 - 4RT_w m''^2_w}}, \quad p_w = \frac{p_\eta + \sqrt{p_\eta^2 - 4RT_w m''^2_w}}{2} \tag{31}$$

and $$\rho_w = \frac{p_\eta + \sqrt{p_\eta^2 - 4RT_w m''^2_w}}{2RT_w}.$$

Finally, assuming negligible radiative heating from the flow, the one-dimensional surface energy balance is given by Eqn. (32),

$$\underbrace{-\kappa_f \frac{dT}{dx}}_{\text{flow conduction}} \underbrace{- \sum_{k=1}^{ns} \rho h_k D \frac{dY_k}{dx}}_{\text{diffusion heating}} = \underbrace{-\kappa_s \frac{dT}{dx}}_{\text{solid conduction}} \underbrace{+ \epsilon\sigma(T_w^4 - T_\infty^4)}_{\text{re-radiation}} \underbrace{+ m''_w \left(h_w - h_s\right)}_{\text{ablation flux}}, \tag{32}$$

where k_f is the effective gas conductivity, h_k is the gaseous species enthalpy, h_w is the mixture gas enthalpy at the wall, h_s is the solid camphor enthalpy at the wall temperature, ϵ is the surface emissivity and σ is the Stefan-Boltzmann constant.

Alternatively, the energy balance equation can be expressed in the form of heat of reaction for the material ablation flux [3]. In this form, the heat diffusion term on the left-hand side is replaced by the sum of mass diffusion fluxes from Eqn. (26), multiplied by the species enthalpies, leading to the following form of the energy balance equation

$$\underbrace{-\kappa_f \frac{dT}{dx}}_{\text{flow conduction}} = \underbrace{-\kappa_s \frac{dT}{dx}}_{\text{solid conduction}} \underbrace{+ \epsilon\sigma(T_w^4 - T_\infty^4)}_{\text{re-radiation}} \underbrace{+ \left[\sum_k h_k m''_k - m''_w h_s\right]}_{\text{heat of reaction}}. \tag{33}$$

This form of the energy balance is more accurate when the set of surface balance equations is solved on the material side. In this case, the computation of the chemical production fluxes at the surface, described in the next subsection, directly accounts for the updated diffusive heating toward the surface. This form of the energy balance was used in the current study.

4.2. Finite-rate ablation

Camphor is a highly volatile material that sublimates at a wide range of temperature conditions prior to melting. For instance, the triple point of camphor is ($T = 453.3$ K, $P = 51,433$ Pa), Ref. [4], which allows testing to be performed at relatively mild hypersonic conditions without reaching the melting point. In this work, the sublimation of camphor is modeled with a Knudsen-Langmuir formulation, that represents a balance between the evaporation and condensation of camphor species at the surface. The sublimation mass flux of camphor is given by

$$m''_c = \alpha \left(p_v - p_c\right) \sqrt{\frac{M_c}{2\pi R_u T_w}}, \tag{34}$$

where p_v and p_c are the vapor and partial pressures of camphor at the wall temperature and α is the experimental vaporization coefficient representing a deviation of surface sublimation rates from the maximum possible value predicted by kinetic theory. In this study, α is assumed to be equal to 0.18 according to Ref. [45]. The partial pressure at the wall is found based on the local pressure and mass fraction of camphor computed from the momentum and mass balance equations. The vapor pressure of camphor is given in the exponential form below as

$$p_v = Ae^{(B/T+C)}, \tag{35}$$

where p_v has the units of (Pa) and T has units of (K). The values of the fitting coefficients A, B, and C are given in Table 11 in the Appendix. It should be noted that the equation for the sublimation mass flux, Eqn. (34) allows for condensation of the material under certain conditions at the wall. Finally, given the sublimation mass flux of camphor, the surface recession rate is found with a simple relation below

$$\dot{s} = \frac{m''_c}{\rho_s}. \tag{36}$$

4.3. Coupling algorithm

In this study, we use an unsteady implicit method with dual time stepping in the NBS-Cart solver which allows for relatively large time steps to be used on the fluid side, on the order of 1×10^{-4} s. With this capability, the material time step is set by the flow solver. To achieve a baseline accurate solution, the material solver performs a single step before updating the boundary conditions. The coupling framework between the two solvers along with the main solution blocks of each domain is presented in Fig. 5. The whole solution procedure can be divided into two distinct phases. The first phase is the convergence of the NBS-Cart solver to achieve a steady-state initial solution for the coupled problem. The second phase starts by interpolating the fluid boundary condition onto the material nodes. Typically a 3-point stencil is sufficient to obtain accurate interpolation. The material solution consists of two main blocks: solution of the surface balance equations and in-depth conduction. Due to the coupled nature of the equations, including the mesh motion, the solution is achieved in an iterative manner as shown in the blue section of the scheme in the figure. The converged system of equations defines the chemical and thermodynamic state and recession at the surface which is interpolated back onto the flow domain.

To accurately model the surface recession, the material solution is evaluated at the surface nodes that compose the NBS grid. Therefore, the recession is directly applied at the nodes and the surface state is interpolated to the face centroids. The material boundary condition is applied directly in the NBS solver whereas the Cartesian solver "feels" this new boundary condition via the overset interpolation. The solution of the flow domain starts by moving the surface grid and interpolating the previous step NBS solution onto the relevant Cartesian cells. Since the Cartesian and NBS domains are solved in a sequential manner, the Cartesian domain is solved first, followed by interpolation and a solution of the near body region. Each flow solver performs a number of pseudo-steps to converge onto the next instant in time. Since the NBS grid resolves the entire boundary layer, the off-body region is less sensitive to the material update, and hence, the NBS solver takes the majority of sub-steps to converge the solution. The operation of the framework is summarized in the algorithm below.

Algorithm 1 Coupled solution advancement procedure. Start from a converged flow solution.

1: Interpolate NBS surface state onto nodes (where the MR solver resides).
2: Solve surface balance equations with in-depth material response.
3: Interpolate MR surface state onto NBS centroids.
4: Move surface grid.
5: Interpolate previous step NBS solution onto relevant Cartesian cells.
6: Solve governing equations on Cartesian grid.
7: Interpolate Cartesian solution onto NBS inflow.
8: Solve governing equations on NBS and advance solution forward in time.

5. Uncoupled framework

5.1. Aerodynamic heating boundary condition

The practical principles for uncoupled simulation of material thermal response problems in the presence of chemically reacting boundary layer were developed during the Apollo era on the basis of film coefficient theory [12,46,47]. In this approach, for equal heat and mass-transfer rates in the boundary layer, the incident conduction and diffusion heat flux toward the surface can be estimated by the enthalpy

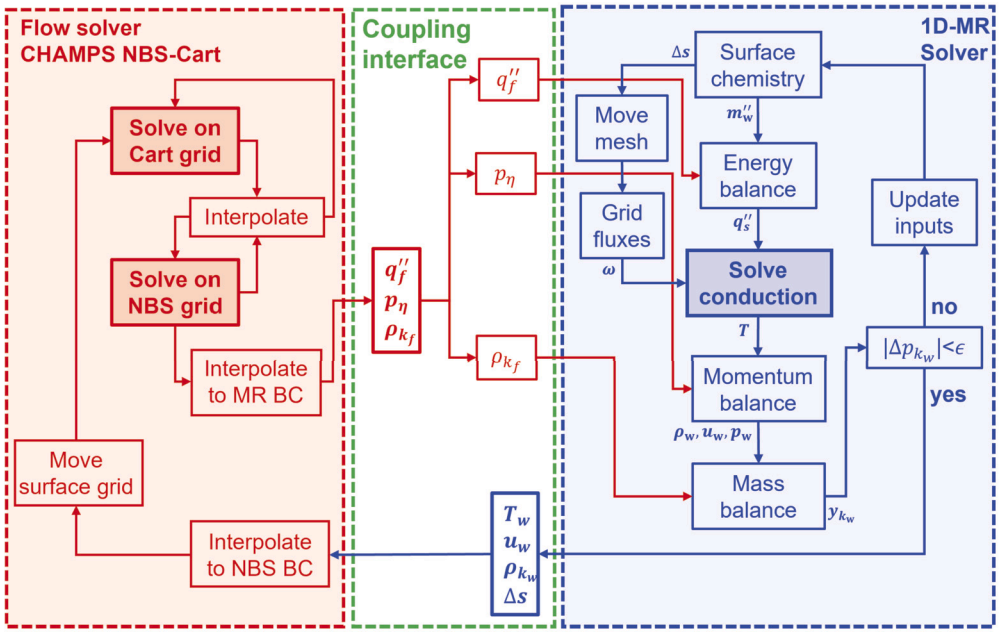

Fig. 5. Coupling diagram between CHAMPS and each 1D-MR solver.

difference between the boundary layer edge and the wall, multiplied by the effective heat transfer coefficient as shown below

$$C_H(h_r - h_w) = -k_s\frac{dT}{dx} + \epsilon\sigma(T_w^4 - T_\infty^4) + m_c''(h_w - h_s), \tag{37}$$

where C_H is the heat-transfer coefficient and h_r is the recovery enthalpy, set here to the free-stream enthalpy of the flow. The heat-transfer coefficient is given in the equation below

$$C_H = C_{H,0}\Omega_{\text{blw}}, \tag{38}$$

where $C_{H,0}$ is the initial ("unblown") heat-transfer coefficient and Ω_{blw} is the blowing correction. The initial heat-transfer coefficient is computed based on the cold wall heat flux and is given in the equation below

$$C_{H,0} = \frac{q_0''}{h_r - h_{w,0}}, \tag{39}$$

where q_0'' is the cold wall heat flux and $h_{w,0}$ is the mixture enthalpy at the initial wall temperature. The blowing correction in Eqn. (38) models the effect of the heat flux reduction due to the blowing of ablating species into the boundary layer and is given in the equation below

$$\Omega_{\text{blw}} = \frac{\Phi}{e^\Phi - 1}, \tag{40}$$

where $\Phi = 2\lambda\dot{m}_c''/C_{H,0}$ and the blowing reduction parameter (λ) is set to 0.5 in this work.

5.2. Equilibrium-based ablation (Bprime)

The alternative way of computing the ablation rate of material in the uncoupled mode is to assume Couette-type flow in the boundary layer and equilibrium conditions. With these assumptions, the ablation rate can be derived by expressing the mass conservation (Eqn. (26)) across the boundary layer as

$$\rho D\frac{(Y_{k,e} - Y_{k,w})}{\delta} + m_k'' = m_w'' Y_{k,w}, \tag{41}$$

where δ is the boundary layer thickness and subscripts "e" and "w" represent the boundary layer edge and wall conditions. Assuming the Couette-type flow, the mass-transfer coefficient is defined as $\rho_e u_e St_m = \rho D/\delta$, where $\rho_e u_e$ is boundary layer edge mass flux and St_m is the mass-transfer Stanton number. By substituting the definition of the mass-transfer coefficient into Eqn. (41) and assuming a single subliming species at the wall (camphor), the mass conservation equation becomes

$$\rho_e u_e St_m \left(Y_{c,e} - Y_{c,w}\right) = m_c''\left(Y_{c,w} - 1\right). \tag{42}$$

Defining a non-dimensional ablation rate of camphor as $B_c' = \frac{m_c''}{\rho_e u_e St_m}$ and assuming zero mass fraction of camphor at the boundary layer edge (no camphor gas in the freestream flow), the non-dimensional ablation rate B_c' is expressed from the above equation in the following simple form

$$B_c' = \frac{Y_{c,w}}{1 - Y_{c,w}}, \tag{43}$$

where $Y_{c,w}$ is the equilibrium mass fraction of camphor gas at the wall conditions.

To find the equilibrium mass fraction of camphor we assume that the partial pressure of camphor is equal to the vapor pressure, given in Eqn. (35) previously. For the given mixture of three species in the system: nitrogen, oxygen and camphor we define the molar fraction of camphor as

$$\chi_c = \frac{p_c}{p} = Y_c\frac{\bar{M}}{M_c} = Y_c\frac{1}{M_c\left(\frac{Y_c}{M_c} + \frac{Y_{N_2}}{M_{N_2}} + \frac{Y_{O_2}}{M_{O_2}}\right)}, \tag{44}$$

where p is the local pressure of the mixture. By assuming a non-reacting flow, the relative mass fractions of nitrogen and oxygen species remain the same through the boundary layer and can be expressed as a function of the mass fraction of camphor as $Y_{N_2} = Y_{N_2,\infty}(1 - Y_c)$ and $Y_{O_2} = Y_{O_2,\infty}(1 - Y_c)$. Substituting the mass fractions of nitrogen and oxygen species into Eqn. (44), the mass fraction of camphor at the wall can be computed as

$$Y_{c,w} = \frac{\chi_{c,w}\left(Y_{N_2,\infty}M_c/M_{N_2} + Y_{O_2,\infty}M_c/M_{O_2}\right)}{1 - \chi_{c,w}\left(1 - Y_{N_2,\infty}M_c/M_{N_2} - Y_{O_2,\infty}M_c/M_{O_2}\right)}. \tag{45}$$

Following the derived non-dimensional ablation rate, the ablation rate of camphor is then given by

$$m_c'' = B_c'\rho_e u_e St_m = B_c' C_M. \tag{46}$$

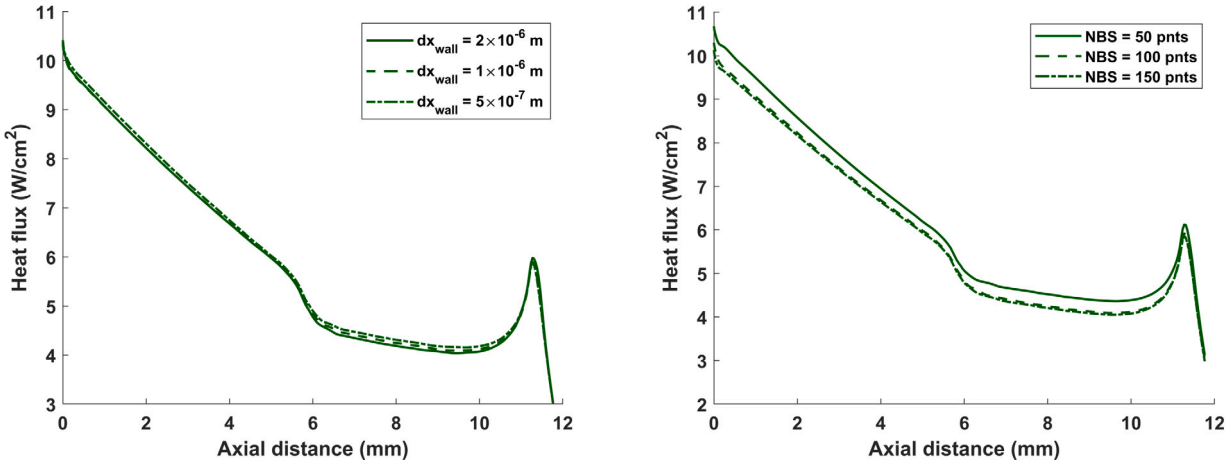

(a) Variable wall spacing (NBS = 100 points). (b) Variable number of NBS points ($dx_{wall} = 1 \times 10^{-6}$ m).

Fig. 6. Test case - 20 bar. Heat flux prediction by NBS-Cart solver under varying levels of near body grid resolution ($T_{wall} = 298.15$ K).

The mass-transfer coefficient C_M, can be found from the Chilton-Colburn relation between the mass- and heat-transfer rate given by

$$C_M = C_H Le^{2/3}, \tag{47}$$

where C_H was defined previously in Eqn. (38).

6. Verification study

6.1. Flow grid convergence study

The grid convergence study was performed using the overset CHAMPS NBS-Cart solver. A schematic of the grid layout for the Phoebus capsule test case was shown earlier in Fig. 3, where the near body Curvilinear grid is overlaid on top of a block-structured Cartesian grid. The mesh of the NBS layer in the figure was intentionally coarsened in both wall-normal and stream-wise directions to make a clear visualization. In general, the NBS layer in this work was set to resolve the entire boundary layer, which makes it possible to perform the grid convergence study by varying only the NBS layer parameters. The grid convergence of the off-body region with the Cartesian mesh is achieved typically automatically by using AMR and the requirement for the mesh refinement level to be high enough to comply with the NBS mesh size in the overset region. The dimensions of the simulated geometry are shown later in Fig. 8(a) with freestream conditions defined in Test 2, presented in Table 2. Apparently, in the overset approach the flow convergence depends on the wall spacing and wall-normal distribution of the nodes in the NBS layer. The study was performed for two scenarios to explore the effect of both parameters and choose the optimal configuration while keeping a constant number of nodes in the streamwise direction, equal to 353. In the first scenario, the NBS layer is fixed to 100 nodes in the wall-normal direction, and the wall spacing is halved from 2×10^{-6} m to 5×10^{-7} m. Fig. 6(a) presents the cold wall heat flux distribution for this scenario, showing a converged solution. In the second scenario, the wall spacing is kept constant at 1×10^{-6} m and the number of nodes in the wall-normal direction is varied in 50-point increments. Fig. 6(b) shows a close agreement for the two finest grids with the stagnation point heat flux differing by less than 2%. Following the performed study, a medium level of refinement (100 nodes) and medium wall-spacing (1×10^{-6} m) was selected as being sufficiently well-resolved and is used for all further simulations.

6.2. Material solver verification based on heat of ablation (Q-star) problem

Verification of the material response solver with the grid contraction scheme was performed using the heat of ablation (Q-star) approach. In this approach, the in-depth material thermal response is modeled with transient heat conduction and surface ablation occurs at a fixed temperature. Mathematically, this problem is modeled using an ablative one-dimensional, semi-infinite material slab with uniform density, constant physical properties and isothermal boundaries. At steady state conditions, the governing equation that characterizes this problem is given below

$$k_s \frac{d^2T}{dx^2} + \dot{s}\rho_s c_{p,s} \frac{dT}{dx} = 0 \quad \text{with} \quad T(x=0) = T_{\text{abl}} \quad \text{and} \quad T(x=\infty) = T_0. \tag{48}$$

Assuming a constant recession rate, the analytical solution to the above equation is given by

$$T(x) = T_0 + (T_{\text{abl}} - T_0) e^{-\dot{s}x/\alpha_s}. \tag{49}$$

To model this problem numerically with the developed solver, the following boundary condition is used in the material response model

$$\left[-k_s \frac{dT}{dx}\right]_s = q'' - \rho_s \dot{s} Q^*, \tag{50}$$

where q'' is the incident heat flux and Q^* is the material heat of ablation. To match the analytical solution given in Eqn. (49), the incident heat flux should satisfy the energy balance at the surface that preserves the fixed ablating temperature. By substituting the analytical temperature profile from Eqn. (49) into the ablating boundary condition, Eqn. (50), the incident heat flux becomes

$$q'' = \rho_s \dot{s} \left[c_{p,s}(T_{\text{abl}} - T_0) + Q^*\right]. \tag{51}$$

To converge to the analytical steady-state solution using the transient heat conduction equation, the material should be sufficiently long to allow for the formation of a steady-state temperature profile. Table 1 shows the verification study parameters, where the only derived quantity in the table is the incident heat flux, which was computed by prescribing the heat of ablation of the material, the fixed ablation temperature and the recession rate.

It should be mentioned that the prescribed recession rate is used only to derive the imposed incident heat flux. In the numerical solution, the recession rate has to be iteratively evaluated to satisfy the fixed surface temperature T_{abl} condition. In this study, an iterative bisection method was used to converge the recession rate to maintain the fixed surface temperature.

The material slab with a length of 3 cm was discretized into 30 cells with a refinement provided by a geometric series with a constant ratio of 1.3. Fig. 7(a) shows the surface recession rate that, after a short transient, converges to the prescribed steady-state value of 0.5 mm/s.

Table 1
Q-star verification study parameters.

Parameter	k_s (W/m-K)	ρ_s (kg/m^3)	$c_{p,s}$ (J/kg-K)	L (cm)	Q^* (MJ/kg)	$\dot{s}$ (mm/s)	T_{abl} (K)	T_0 (K)	q'' (W/cm^2)
Value	0.4	1500	1500	3	1	0.5	1100	300	165

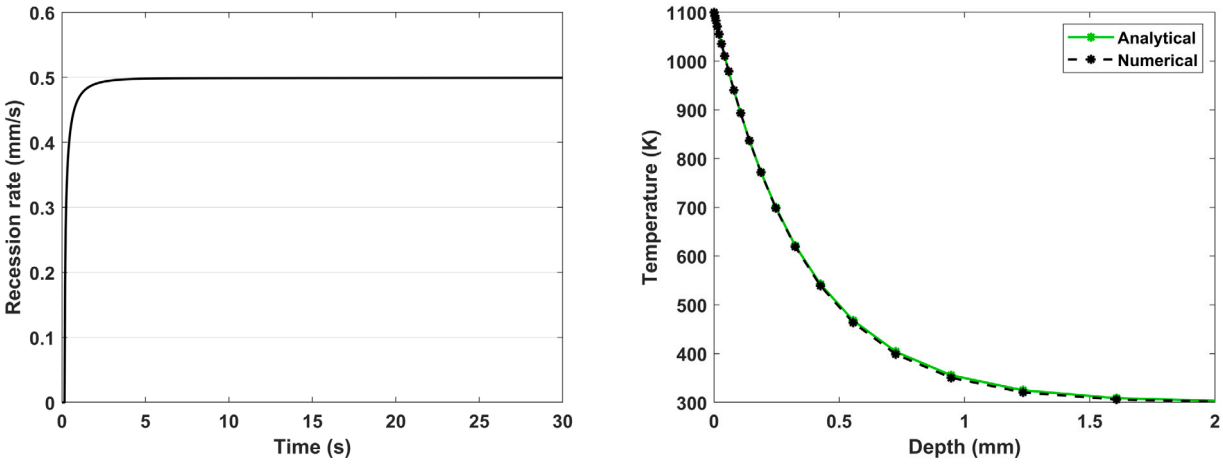

(a) Steady state recession rate (b) Steady state temperature profile

Fig. 7. Verification of contracting 1-D mesh algorithm.

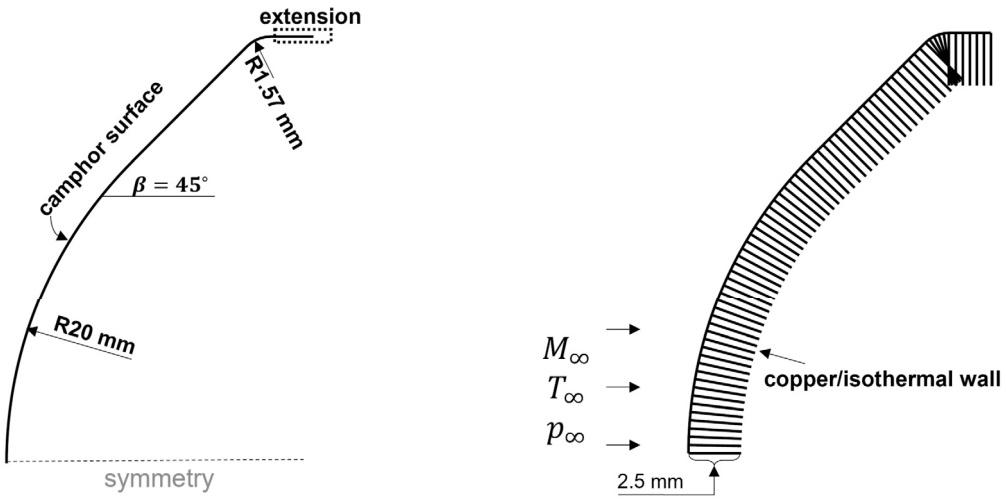

(a) Geometry dimensions (b) Camphor layer discretized with 1D rays.

Fig. 8. Sub-scale Phoebus capsule geometry and camphor layer setup.

Fig. 7(b), shows the in-depth steady-state temperature profile that was obtained once the recession rate reached the steady state. A close match can be seen with the analytical solution from Eqn. (49). A slight mismatch between the approaches results from the discretization of the slab and likely the length of the domain to maintain semi-infinite slab conditions. The maximum error with respect to the analytical solution is 0.6%. It should be mentioned that due to surface recession, the temperature profile was translated with the recessing boundary. To compare the profile to the analytical solution, the numerical solution was shifted to the origin.

7. Problem description

Validation of the coupled framework between CHAMPS and a network of 1D-MR solvers is based on the experimental campaign presented in Refs. [31,32]. In the experiment, a sub-scale Phoebus capsule made of copper was covered by a layer of camphor and exposed to Mach 6 flow in a hypersonic H3 facility at VKI. The experiment was performed at multiple total pressure conditions and included a photogrammetry setup to track camphor surface recession over time. The test article in the experiment is a spherically-blunted cone with a 20 mm nose radius, 45 degrees cone half-angle, 0.157 mm shoulder radius, and 20 mm front radius as shown in Fig. 8(a). In the simulation, the geometry is represented by an axisymmetric shape with an added extension behind the shoulder. The extension is not part of the original geometry and was added to provide extra sampling points at the domain edge for the fluid solver. The material is discretized with a network of one-dimensional solvers, called rays in this study. Fig. 8(b) shows the discretization of the camphor layer with 1D rays. The total number of rays is 353, however, in the figure, the number of rays was reduced for clarity. It can be seen in the figure that due to the small radius of the shoulder, the material rays intersect in this region at approximately 60% of the lo-

Table 2
Phoebus capsule experimental and simulation conditions [32].

	Test 1	Test 2	Test 3
p_0 (bar)	15.65	20.57	25.66
T_0 (K)	524.8	487.2	511.0
Mach	6	6	6
u_∞ (m/s)	962.1	927.0	949.4
p_∞ (Pa)	991.0	1302.8	1625.2
T_∞ (K)	64	59.4	62.3
ρ_∞ (kg/m^3)	0.053956	0.076402	0.090868
T_{wall} (K)	298.15	298.15	298.15
Y_{N_2}	0.767	0.767	0.767
Y_{O_2}	0.233	0.233	0.233
Y_{cmp}	1×10^{-10}	1×10^{-10}	1×10^{-10}
Duration (s)	30	30	30

cal thickness. The intersection of the rays is expected to deteriorate the accuracy of the solution at the shoulder. However, the corruption of the solution would happen only later in the simulation, due to the thin thermal layer forming in low-conductivity materials such as camphor. As reported in Ref. [32], camphor was applied with a uniform thickness of 2.5 mm on top of a copper holder. The exact geometry of the copper holder was not provided, instead, a uniform thickness of 2 mm was assumed, corresponding to the thickness of the holder in the stagnation region [48]. In general, simulation of high-conductivity materials such as copper with 1D solvers is not accurate, due to the strong conduction in the lateral direction. The inclusion of copper in the current study was done to justify the assumption of isothermal wall boundary conditions for future studies. Each camphor layer ray is discretized with 50 cells with geometric spacing and a minimum wall spacing of 1×10^{-6} m, identical to the fluid side. The copper layer is discretized with 10 cells with uniform spacing.

All rays were discretized using the same geometrical factor for a rectangular geometry (m = 0 in Eqn. (24)). The reason for that was an instability observed in the flow solution in the transition regions between the sections of the geometry, such as the nose, cone, and shoulder. Using different geometrical factors for the geometry representation potentially led to a discontinuity in the surface response along the joints of the sections, causing a gradual growth of instability, and corrupting the flow and material solution. The simplification to a constant geometrical factor is based on two assumptions: (1) the thin thermal layer in camphor as a result of the low conductivity of the material and (2) insignificant deviation of the cross-sectional area of each ray from the rectangular geometry. For the nose and conical sections, the ratio of the stack-up thickness to the radius of the geometry is 2/9, allowing for the assumption of a low effect of the cross-sectional area change on the final solution. For the shoulder region, the assumption of a rectangular cross-section would not be valid due to the intersection of the rays. This introduces additional inaccuracy in the solution in this region.

The numerical simulations were performed at three total pressure conditions and are presented in Table 2 above. All three experiments were performed for 30 s, however, the stagnation and shoulder region ablated faster and reached the copper sub-structure earlier [32]. In the experiment, no temperature measurements were performed of the material or environment. As an assumption, the ambient and initial temperature of camphor was assumed equal to 298.15 K. The same temperature was assumed at the back wall of the copper holder.

In addition to the coupled simulations, uncoupled material simulations with applied aerodynamic heating and equilibrium thermo-chemistry conditions were performed for reference. The uncoupled simulations were performed only at the stagnation point. The aerodynamic heating parameters were computed based on the cold wall heat flux and assuming a unity Prandtl and Lewis numbers for the recovery enthalpy. Table 3 summarizes the derived aerodynamic heating parameters. The equilibrium thermo-chemistry was computed using Eqn. (43) and Eqn. (45) for a range of pressure and temperature values expected in the simulation. Fig. 9(a) shows the non-dimensional ablation rate and Fig. 9(b) shows the wall mixture enthalpy computed with respect to standard conditions.

Table 3
Stagnation point aerodynamic heating parameters.

	Test 1	Test 2	Test 3
q_0'' (W/cm^2)	10.84	10.32	13.0
p_w (kPa)	46.33	60.66	75.97
$h_r = h_0$ (J/kg)	524,403	491,461	511,847
$h_{w,0}$ (J/kg)	-9029	-7041	-5625
$C_{H,0}$ (kg/m^2-s))	0.203	0.207	0.251

8. Results

In this section, numerical results from the three test cases at 15, 20, and 25 bar are presented and compared to the reference numerical and experimental data. The baseline coupled solution is obtained by coupling the two solvers after every physical material time step. The material step is set to 2.3×10^{-4} sec, corresponding to the fluid Courant–Friedrichs–Lewy condition of 10,000. The baseline simulation uses camphor gas transport properties from the database compiled by Yaws [37–39]. Additional simulations explore the effect of alternative transport property models, the type of boundary condition, and the influence of "decoupled" material steps on the solution accuracy.

8.1. Validation of the coupled framework

Fig. 10 shows the temperature and velocity contours of the flow-field at 0 and 30 s for the 20 bar case. Significant recession and shape change of the geometry can be observed in the bottom half of the figures. The original shoulder region completely smooths away, changing the local temperature and velocity distribution. The AMR algorithm used to refine the mesh around the shock and the wall accurately tracks the shock displacement as a result of surface motion.

The next set of plots in Fig. 11 shows the time evolution of the surface quantities such as conduction flux, temperature and mass blowing in the 20 bar case simulation. All graphs are plotted as a function of the initial axial length of the geometry and the vertical dashed lines mark the transition between the geometrical sections. It was observed that a cooling effect of the copper holder starts to appear at around 12 s in the stagnation region after the start of the simulation and leading to the change in the trend of the surface quantities. To show the trend in the data, the plotted results are split into two rows: the upper row - "heating" phase, duration 0 to 12 s and the bottom row - "cooling" phase, duration 12 to 30 s. It can be seen from the first row, that rapid heating of the material surface occurs in the first 0.5 s, leading to a drastic drop in the conduction heat flux and a rapid increase in the surface temperature and mass blowing. In the course of the first few seconds, the initial heating spike at the transition from the conical to the shoulder sections leads to an increased ablation and smoothing of the shoulder curvature and subsequently smoothing away the initial heating spike. This interaction between the applied boundary conditions and the topology change is accurately captured in the coupled simulation.

The bottom row of the figures shows the "cooling" trend in the surface quantities. Once the material becomes thin enough, especially in the stagnation region and shoulder, the thermal effect of the copper back structure comes into play. The surface temperature starts to gradually drop (Fig. 11(e)), leading to a gradual increase in the conduction flux, but a massive decrease in the mass blowing. The rapid decrease in the mass blowing is caused by the exponential nature of the vapor pressure of camphor, Eqn. (35), in the sublimation process. A small decrease in the surface temperature leads to a large decrease in the vapor pressure, decreasing the vapor to the partial pressure difference and subsequent decrease in the sublimation mass flux, Eqn. (34).

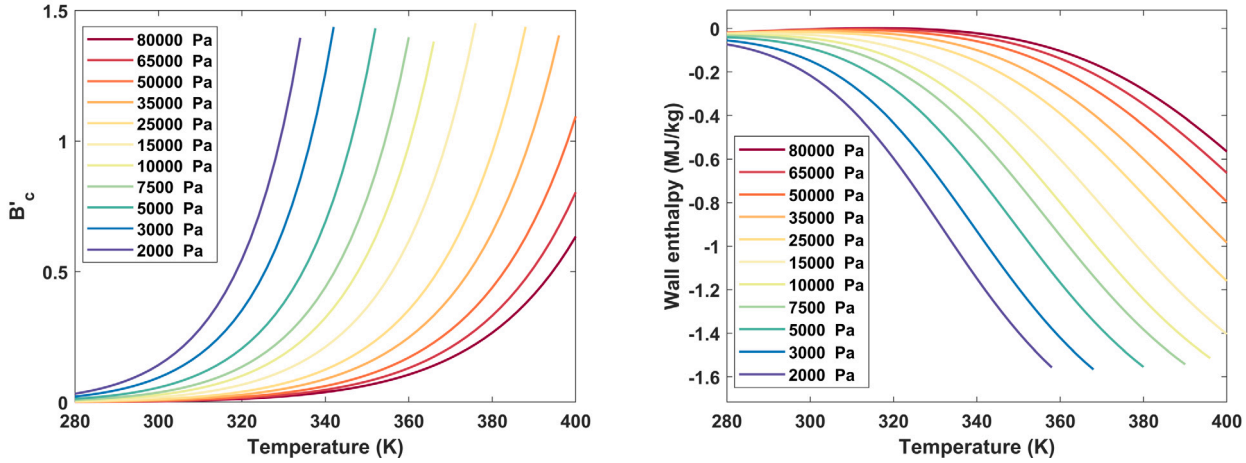

(a) Non-dimension camphor ablation rate. (b) Mixture wall enthalpy.

Fig. 9. Equilibrium-based camphor ablation thermochemistry.

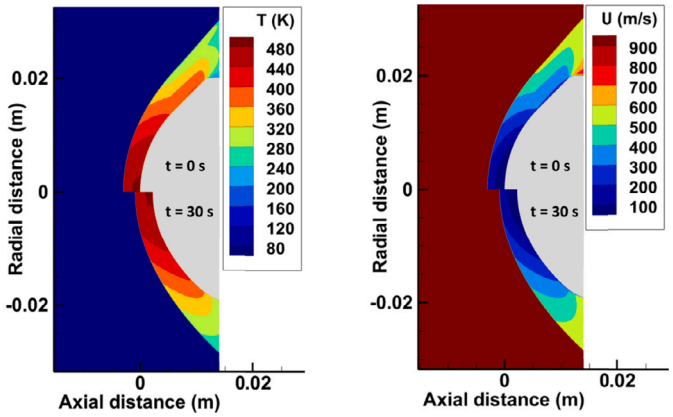

(a) Temperature contours. (b) Axial velocity contours.

Fig. 10. Test case - 20 bar. Flow-field around capsule at 0 s and 30 s.

Fig. 12 shows the time evolution of surface pressure which is an indicator of the continuous topology change. It can be seen that the initial pressure distribution significantly changes as the surface ablates. The sharp transitions of pressure between the geometrical sections of the geometries are smoothed away.

The next set of figures presents the comparison of the numerical data to experiments. Fig. 13 shows the comparison of the stagnation point recession between the experiment and three different numerical approaches. The solid curve represents the coupled results, obtained with the finite-rate (FR) ablation model and diffusion coefficient from Yaws. The dashed curve represents the uncoupled results, simulated using the equilibrium (EQ) B-prime ablation model and the assumption of equal heat- and mass-transfer coefficients. Finally, the dotted curve represents the steady-state results obtained by Bianchi et al. [32]. An excellent agreement is seen between the coupled results and the stagnation point experimental data at all three pressure conditions. The “cooling” effect of the copper holder is clearly seen in the results, where the recession rate starts to decrease after enough material has ablated away and the cold thermal mass of copper starts to “sink” the heat from the surface. The uncoupled simulation shows a different trend than the coupled approach. The amount of recession stays within the experimental uncertainty in the first 6 to 10 s, depending on the pressure condition, but later deviates from the measurement and matches again only after all material has ablated away at the stagnation point at around 23 - 28 s. The steady-state simulation appears to follow the uncoupled curve data, but due to the lack of cooling effect by the copper wall, the solution predicts a constant ablation rate and eventually significantly deviates from the experimental data. It should be mentioned, that the steady-state simulation, performed in the reference study, used different transport properties of camphor, that presumably were higher in magnitude than those used in the current study. The effect of the transport properties will be shown later, but for the sake of comparison, the different trend in the steady-state data occurs not only from the lack of the back wall cooling but also from the difference in the transport properties.

Fig. 14 shows the comparison of the predicted recessed shape of the geometry predicted with the coupled approach and the one measured in the experiment with a photogrammetry technique. The reference data includes profiles at 11 s from the start of the experiment for all three cases and an additional profile at 19 s for the 20-bar case. Similarly to the previous set of results, the shape change of the geometry agrees exceptionally well with the experimental data for most of the geometry, given that the measurement contains uncertainty. Observing the shoulder region, smoothing of the initial curvature can be seen already in the 11 s profiles. Additionally, due to the local peak in the heating rate, seen in Fig. 11(a), the increased ablation rate leads to a small concave surface in the shoulder region which is more visible in the 19 s profile, 20 bar case. The concave surface seems to align with the experimental shape, but it is hard to compare the data with full confidence, due to the measurement uncertainty and digitization of the experimental data.

To explore further the performance of the uncoupled approach we plot in Figs. 15(a) and 15(b) the distribution of surface temperature and recession extracted at 11 s and 19 s in the 20-bar case. It can be seen, that both plotted quantities strongly deviate from the prediction of the coupled approach. The deviation in the stagnation region appears to be related to the inaccurate model of the heat and mass transfer coefficients since the stagnation region barely experiences non-equilibrium conditions [29] and the shape change effect is minimal. Away from the stagnation region, the non-equilibrium conditions and shape change take a stronger effect, peaking in the shoulder region. For example, ablation of the shoulder leads to a local redistribution of the heat flux, smoothing the initial spike and increasing the heating in the exposed post-shoulder region as seen in Fig. 11(a). Mainly due to this fact, the uncoupled approach predicts drastically lower temperatures and the amount of recession in the post-shoulder region.

8.2. Sensitivity analysis

This section presents a sensitivity analysis with respect to the different transport properties of the camphor gas, the type of back wall boundary condition, and the coupling procedure between the solvers.

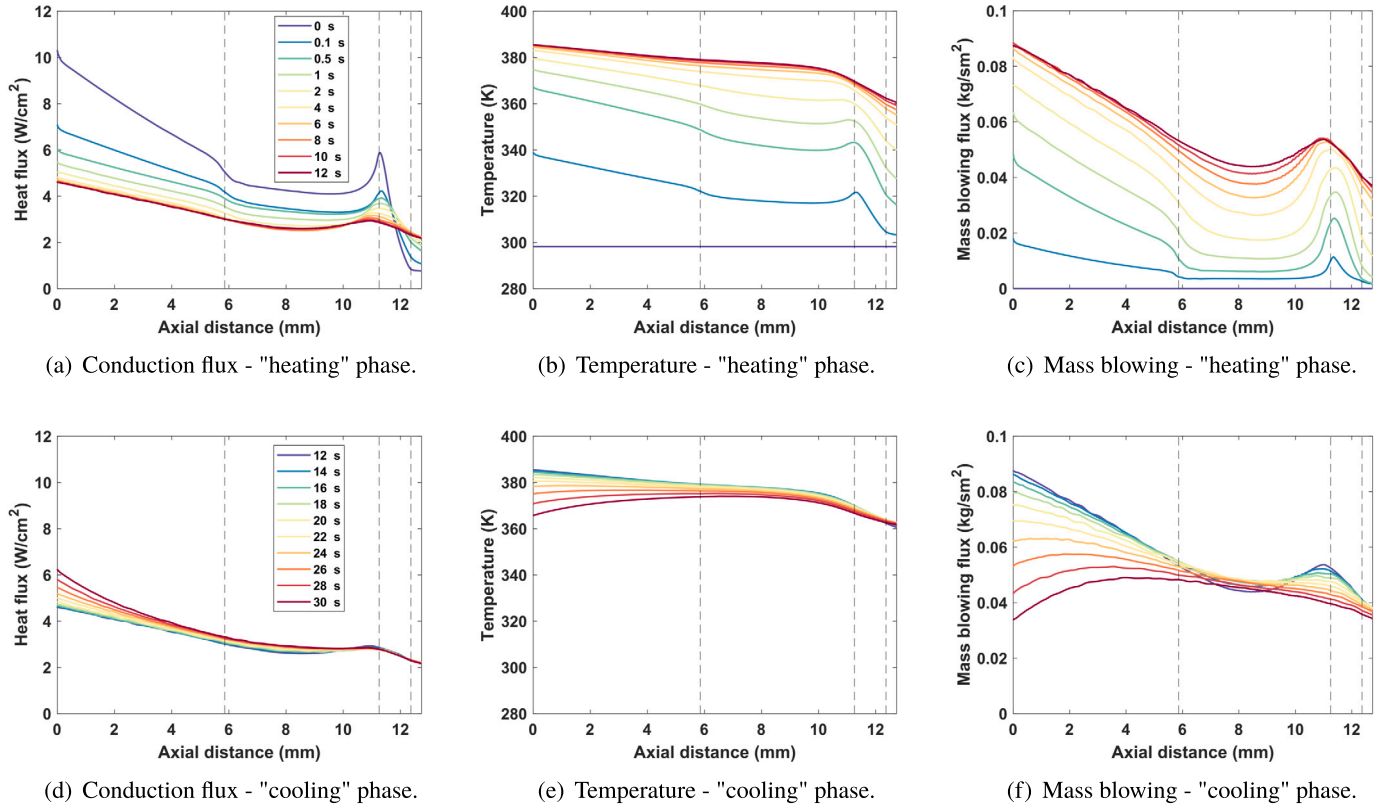

(a) Conduction flux - "heating" phase. (b) Temperature - "heating" phase. (c) Mass blowing - "heating" phase.

(d) Conduction flux - "cooling" phase. (e) Temperature - "cooling" phase. (f) Mass blowing - "cooling" phase.

Fig. 11. Test case - 20 bar. Distribution of surface quantities around the capsule. Figures are split into “heating” and “cooling” phases. Axial distance is set to the initial length of the geometry.

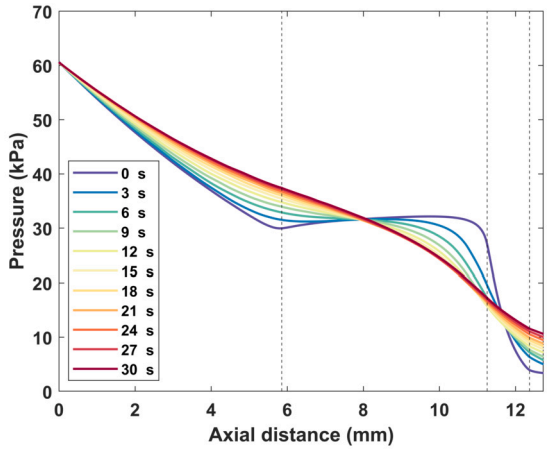

Fig. 12. Test case - 20 bar. Pressure distribution.

8.2.1. Effect of transport properties and type of boundary condition

One of the challenges in modeling ablation problems lies in the uncertainty of estimation of the transport properties of the individual species and their mixture [49]. Uncertainty in the mixture conductivity and viscosity would affect the heating to the surface, while uncertainty in the diffusion model would affect the diffusion heat flux and the ablation rate of the material. In this study, camphor gas transport properties were obtained from two different sources. In the literature, the data was found in the handbook of Yaws for organic and in-organic gaseous substances [37–39], providing a baseline property model in this study. The alternative transport data was obtained using the quantum chemical simulation performed by Haskins [40], where the dynamics of the camphor molecule were modeled based on first principles. Fig. 16 shows the comparison of the stagnation point recession between the Yaws and Haskins transport property models. The Haskins model predicts slightly better agreement with the experimental data compared to Yaws’ model and agrees better with the final thickness of the material. In the 15 and 20-bar cases, the improvement in the prediction is higher compared to the 25-bar case. This result follows directly from the higher diffusion coefficient predicted by the QC simulation at lower pressures, (Fig. 2(b)).

In general, the data for transport properties of each individual species in the mixture is not always available or requires complex computer simulations to obtain one [50]. The diffusion transport, directly responsible for the ablation rate of the material, is commonly modeled with a constant Lewis number assumption in the absence of more accurate models. In this study, we present an additional set of simulations, showing the effect of Lewis number assumption on the ablation rate of the material.[4]

Fig. 17 shows the comparison of the baseline solution with Yaws’ transport properties to the simulations, where conductivity and viscosity were modeled with the Yaws’ model, but the diffusion coefficient was modeled with a Lewis number of 1.0 and 1.4. This way, we can observe the sensitivity of the solution to the diffusion model. First, we see that the change in the diffusion coefficient has a substantial effect on the ablation rate, where the Lewis number approach predicts a higher rate, compared to the Yaws model. The difference between the value of 1.0 and 1.4 is less substantial. Second, the coupled results with the Lewis number of 1.0 and 1.4 get closer to the uncoupled data but are still unable to match the obtained uncoupled solution. As was suggested earlier, the strong deviation of the uncoupled approach is attributed to the inaccurate model of the heat- and mass-transfer coefficients that directly affect the heating and ablation rate at the material surface. The fact that the diffusion model with a Lewis number of 1.0 and 1.4 is

[4] note that the Lewis number in this study and in the hypersonic community, in general, is defined as a ratio of mass and thermal diffusivity.

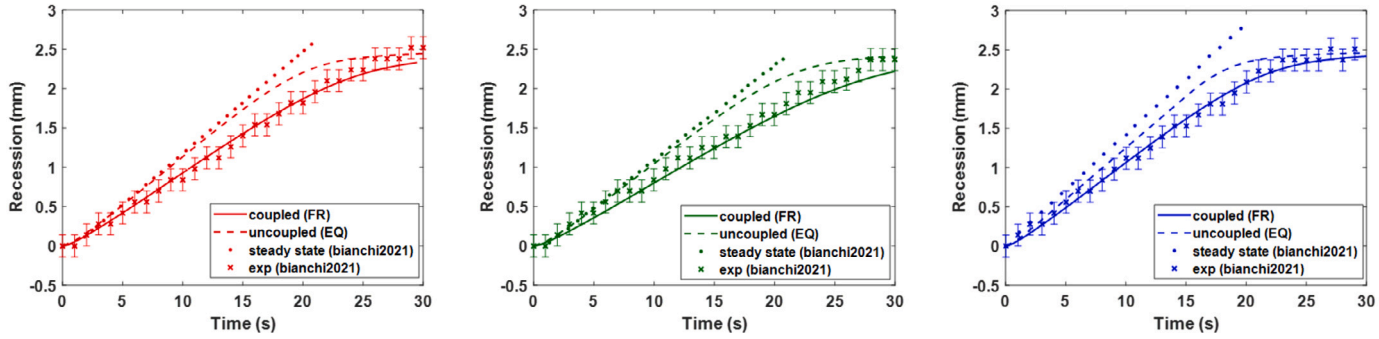

(a) Test case - 15 bar. (b) Test case - 20 bar. (c) Test case - 25 bar.

Fig. 13. Comparison of the stagnation point recession profiles with available numerical and experimental data.

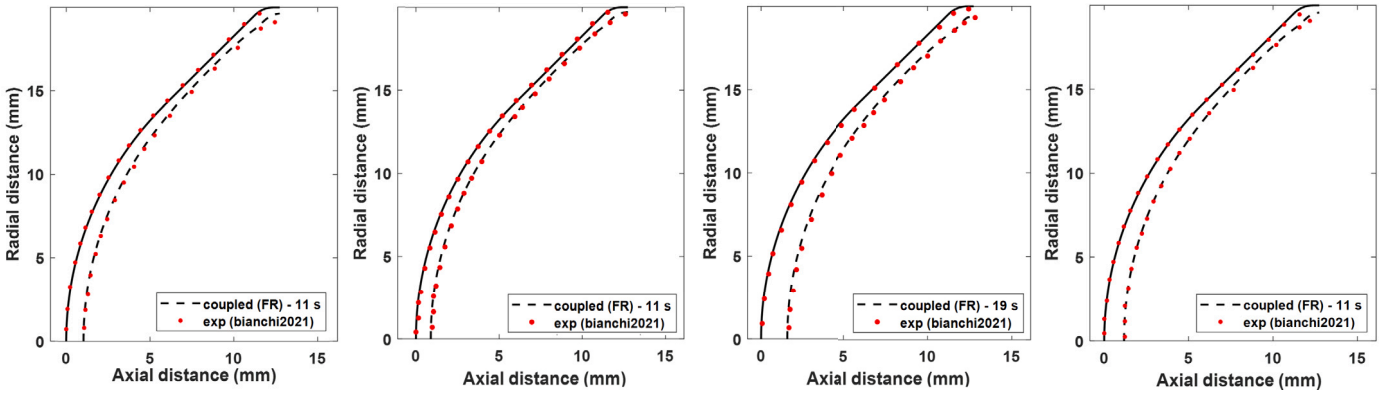

(a) Test case - 15 bar (b) Test case - 20 bar (c) Test case - 25 bar

Fig. 14. Comparison of recession shape predicted with coupled approach and experimental measurement.

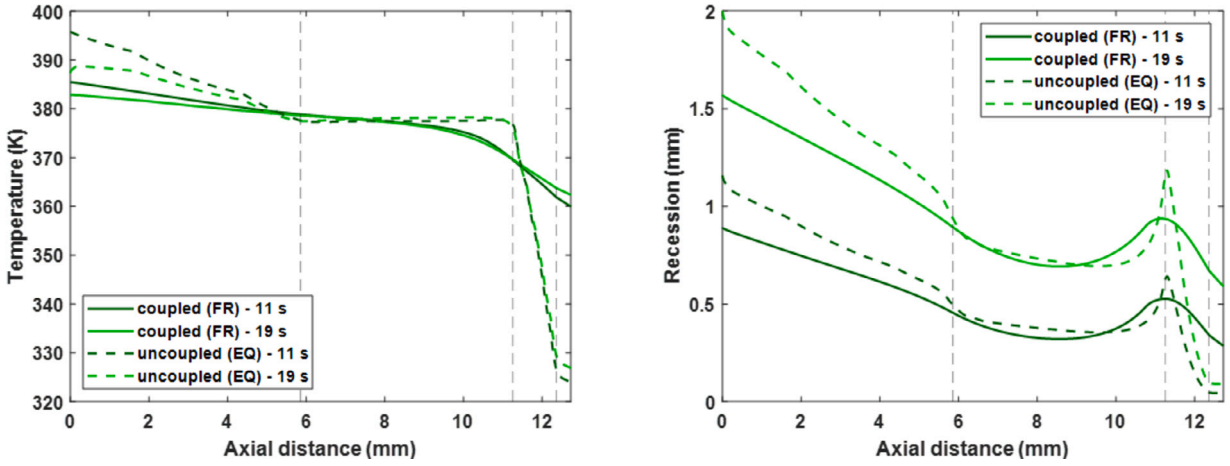

(a) Surface temperature. (b) Surface recession.

Fig. 15. Test case - 20 bar. Comparison of coupled (finite-rate) and uncoupled (equilibrium) solutions at 11 s and 19 s.

still far from the prediction of the uncoupled approach points to the more complex behavior of the local transport properties. Further analysis of the deviation of the uncoupled approach is outside of the scope of the current work and is explored in detail in the follow-up study [51].

Another common assumption in the simulation of ablation problems is the type of boundary condition at the back wall of the material. Usually, the tested materials are either highly insulative and thick or in addition mounted on a highly insulative material such as LI-2200. Under such conditions, the assumption of an adiabatic back wall is reasonable. In the current case, however, the camphor thickness is only 2.5 mm and it is applied on a copper holder, which acts as a strong heat sink. Fig. 18 shows the effect on the recession rate if the back wall was assumed to be adiabatic. For a duration of around 12 s, the stack-up case with copper and the adiabatic wall case is perfectly aligned, however, at the residual material thickness of around 1.5 mm, the two curves start to show the opposite trend. The recession rate in the adiabatic case starts rapidly increasing and very quickly most of the material ablates away, while in the copper stack-up case the recession rate gradually decreases and conforms with the experimental data.

To show the cooling effect of the copper holder and justify the use of isothermal boundary conditions in future studies, the in-depth tem-

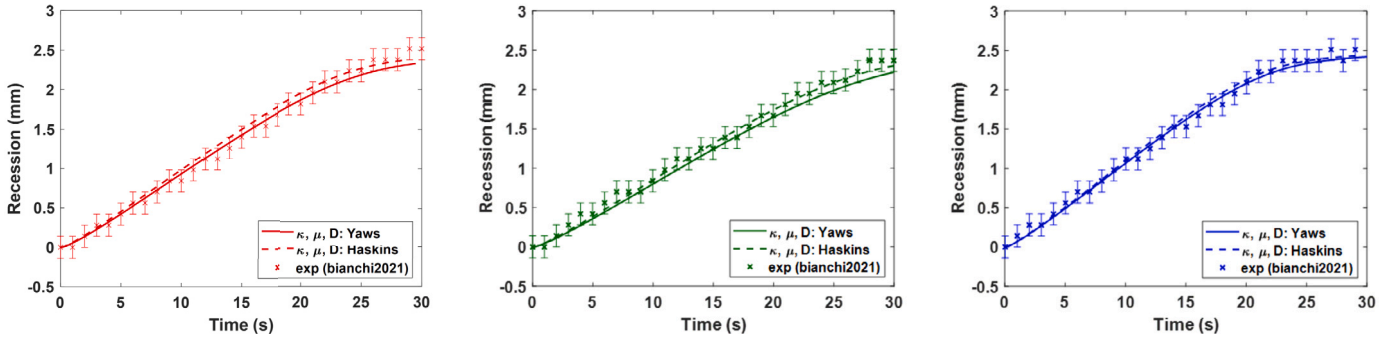

(a) Test case - 15 bar (b) Test case - 20 bar (c) Test case - 25 bar

Fig. 16. Effect of Yaws and Haskins transport properties on stagnation point recession prediction.

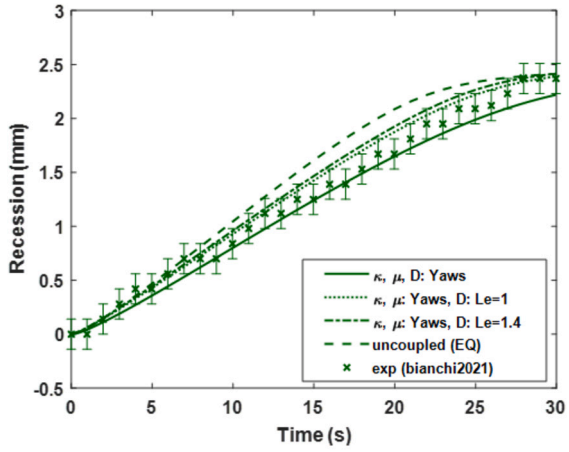

Fig. 17. Test case - 20 bar. Effect of diffusion coefficient on stagnation point recession.

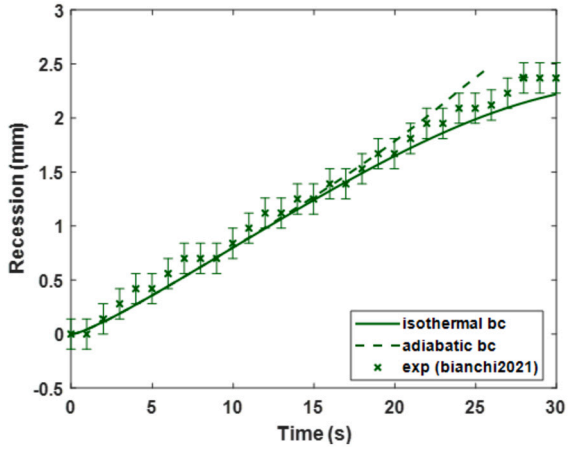

Fig. 18. Test case - 20 bar. Effect of adiabatic wall boundary condition on stagnation point recession.

perature profiles inside the stagnation ray are plotted in Fig. 19(a). It can be seen that as the ablation front (axial displacement of the temperature profiles) advances, the surface temperature reaches a maximum and then gradually goes down as less and less material remains. In addition, the temperature rise at the camphor-copper interface appears to be only a fraction of a degree, indicating that an isothermal wall assumption would be a reasonable choice in this study. In contrast, Fig. 19(b) shows the in-depth temperature distribution in the adiabatic wall case. The lack of cooling by copper leads to extreme heating of the residual material when almost the entire piece is at the same high temperature.

8.2.2. Effect of coupling procedure

As described earlier in section 4, to account for the dependence of surface balance equations on the surface temperature, the balance equations were solved iteratively with the solution of the conduction equation and grid motion. In the current, one-dimensional framework of the material solver, the cost of moving the mesh and solving the linear system is very low. However, in two- and three-dimensional problems motion of the mesh and the solution of the governing equations typically requires the inversion of the linear system, which adds a significant cost to the computation. Finally, the convergence of the iterative loop with the energy equation is a more complex system and not always a trivial task that might require additional resources to converge the solution. Thus, it is of high importance to check the sensitivity of the solution to the iterative procedure. Fig. 20 shows a comparison between the fully iterative and a semi-iterative procedure, where the solution of the conduction equation and mesh motion is excluded from the iterative loop. In this case, the surface temperature is assumed constant during the iteration, taken from the previous time step and the conduction equation along with mesh motion is solved once after the surface balance loop has converged. The curves in the figure correspond to four points on the material surface, stagnation (ray - 1), middle of the nose section (ray - 75), middle of the conical section (ray - 225) and the first point on the shoulder (ray-302) that also corresponds to the spike in the heat flux seen in Fig. 11(a).

Following the surface temperature and recession curves in Fig. 20, it is evident that the solution is very similar between the fully-iterative and semi-iterative procedures, with only a small difference at the shoulder ray. This outcome is very advantageous, as it allows for savings on the computational cost of inverting the linear system and performing mesh motion during the surface iteration loop. However, extrapolating this outcome to the higher heating rate cases should be done carefully. At higher heating rates, the surface temperature increases much faster and the assumption of constant temperature within the surface iterative loop could lead to inaccuracy in the prediction of ablation mass flux and hence, the energy balance at the surface. It should be also mentioned, that the step size of the material solver would have an additional effect on the accuracy of the method. An increase in the time step would lead to a larger material state change per step and hence, the lack of temperature update in the iterative loop could lead to larger errors.

The computational time of the coupled simulation could be further improved if the flow and material solvers were allowed to be called at different frequencies. Stepping the material solver with a larger time step or sub-stepping the solver multiple times before exchanging the boundary conditions with the flow solver would speed up the advancement of the physical time of the problem. In the last part of this study, we explore the effect of the coupling frequency between the solvers on the solution accuracy and computational time of the simulation. We compare the baseline solution, where the two solvers exchange the boundary conditions every step, to the approach where the material solver is allowed to sub-step multiple “decoupled” steps before

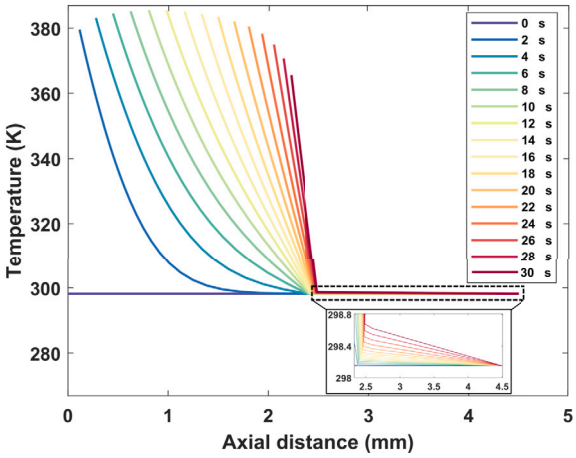

(a) Temperature distribution in the stack-up case with the isothermal wall.

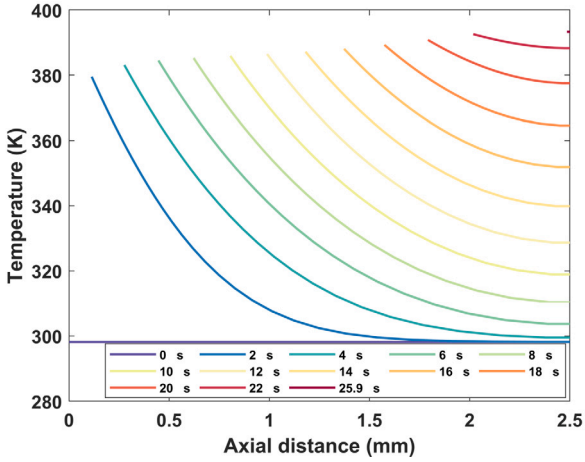

(b) Temperature distribution with adiabatic wall.

Fig. 19. In-depth temperature profiles in isothermal and adiabatic boundary condition cases.

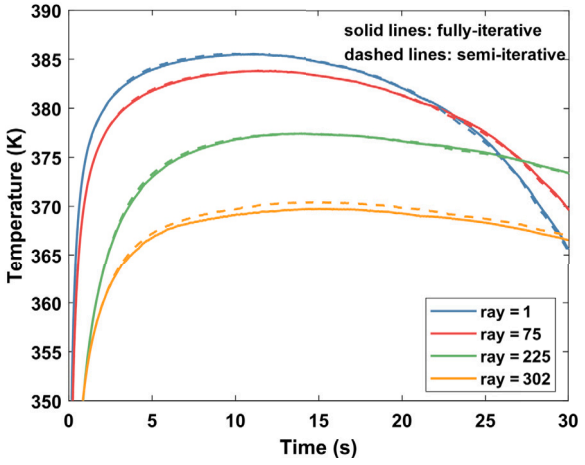

(a) Temperature time history.

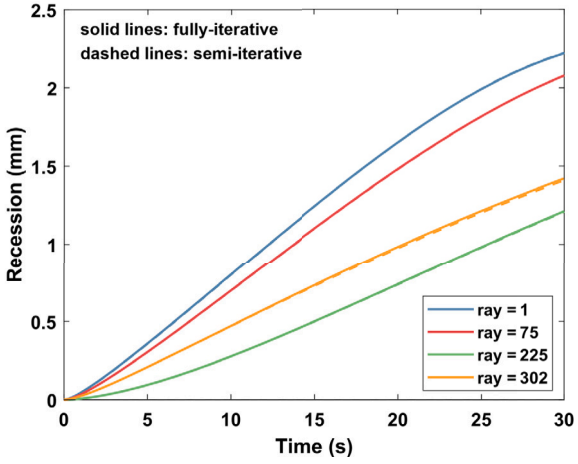

(b) Recession time history

Fig. 20. Test case - 20 bar. Effect of exclusion of conduction solver and mesh motion from the surface balance loop (see Fig. 5).

exchanging the boundary conditions with the flow solver. To compare the results to the baseline solution, we fix the maximum allowed number of the fluid sub-steps used to re-converge the solution after every exchange of the boundary conditions. Figs. 21(a) and 21(b) show the temperature and recession time histories for the different number of "decoupled" material sub-steps. Specifically, the material solver is allowed to sub-step 2, 5, and 10 steps, compared to the baseline solution. With this approach, the relative duration of the simulation has decreased by 11.3% in the 1/2 case, 50.5% in the 1/5 case, and 62.9% in the 1/10 case. The reduction in the simulation time between the 1/1 and 1/10 cases is quite significant but is clearly non-linear with the number of material sub-steps. The non-linearity occurs as a result of the increased number of flow solver sub-steps to achieve re-convergence. To clarify, as the simulation proceeds further, the change in the material state happens at a slower rate, leading to the faster re-convergence of the flow solver. By increasing the number of material sub-steps, the change in the material state becomes larger per exchange step of the boundary conditions with the flow solver. This leads to a larger number of the fluid sub-steps to re-converge the solution before reaching the threshold. As a result, the expected decrease in the overall computational time due to material sub-stepping is adversely affected by the increased number of fluid sub-steps performed for re-convergence.

In terms of the solution accuracy, we observe that increasing the material sub-steps increases the relative error of the solution. The behavior of the error in the temperature profiles is not monotonic, since the material experiences the "heating" and "cooling" phases and the effect of "decoupled" material sub-steps is alternating. The temperature tends to be underpredicted in the "heating" phase and overpredicted in the "cooling" phase. Overall, however, the average relative error in the 1/10 stepping case is still very small and is less than 0.5%. The error in the amount of recession is reported at the end of the simulation for the 1/10 stepping case and appears to vary between 2.8% at the stagnation ray to 6.9% at the ray on the conical section of the geometry. The increase in the recession error in the conical region appears to be consistent with the temperature error increase in this region. Interestingly, the highest error appears to be in the lower heating region on the geometry and the error in the stagnation region is the lowest.

Given the advantage of reducing the duration of the simulation with material sub-stepping, the accuracy of the solution can be improved by introducing a variable time-stepping. In the simplest approach, during the initial transient heating phase, the exchange frequency between the solvers can be identical. As the change in the surface temperature or recession rate per time step decreases, the material can start taking a larger number of sub-steps. A more robust methodology for controlling the number of sub-steps or the size of the material step can

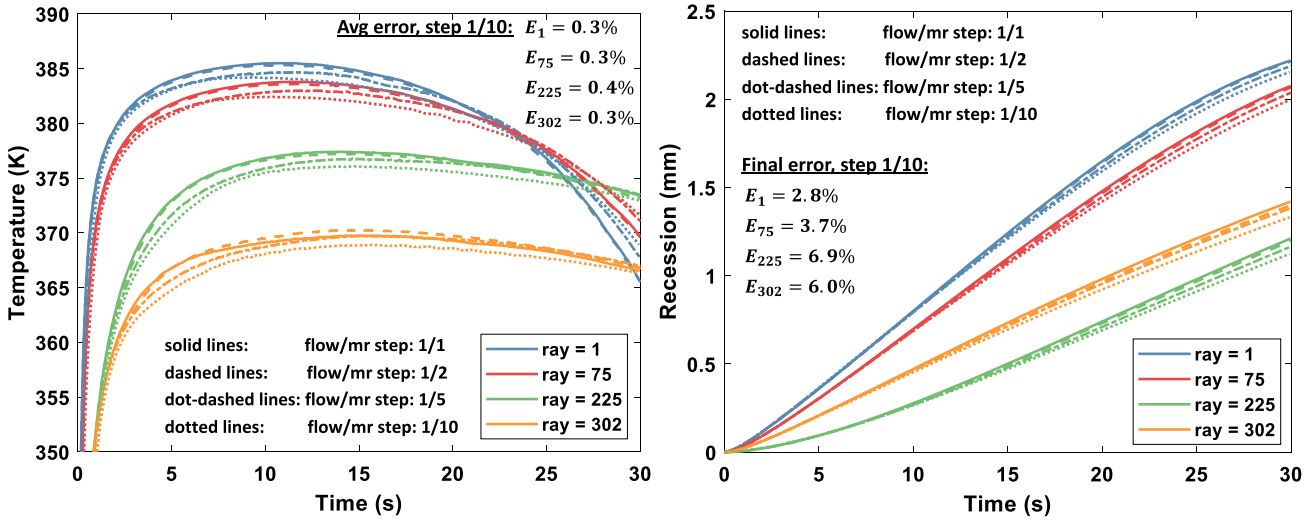

(a) Temperature time history.

(b) Recession time history

Fig. 21. Test case - 20 bar. Effect of "decoupled" stepping frequency between the flow and material solvers.

be done with the help of control theory and the use of proportional-integral-derivative controllers as suggested in Ref. [52]. In this work, exploration of the variable stepping methods is left for future studies.

9. Conclusions

In this study, we presented a coupled framework between the NBS-Cart hypersonic flow solver within CHAMPS and a network of one-dimensional material solvers with surface ablation. We verified the newly developed material response solver by solving the heat of ablation problem and ensuring the correct implementation of the moving boundary condition. The validation of the coupled framework was performed by comparing it to a low-temperature ablation experiment under different freestream conditions. The results showed excellent agreement with the recession of the stagnation point and the overall shape change of the geometry.

A sensitivity analysis was conducted to investigate the influence of transport properties of camphor species on the ablation rate. The analysis revealed a strong dependence on the diffusion model, which partly explained the significant deviation observed in the uncoupled results. Additionally, we found that the copper holder behind the camphor layer had a significant impact on accurately predicting the material ablation rate. Furthermore, the sensitivity study on the back wall boundary conditions confirmed that an isothermal back wall assumption was appropriate for this problem.

Finally, we explored the effect of the coupling procedure between the two solvers. Excluding the solution of material conduction and mesh motion from the surface balance loop had minimal impact on the solution accuracy, as expected due to the small time step used for advancing the material solution. Alternatively, increasing the frequency of material solver steps compared to the flow solver resulted in an increased error in surface temperature and recession. The maximum error in recession reached approximately 7% in the case with 10 material response solver sub-steps. However, increasing the number of material sub-steps led to a decrease in the overall computational time by approximately 63% in the case with 10 material sub-steps.

CRediT authorship contribution statement

Aleksander L. Zibitsker: Investigation, Methodology, Software, Validation, Writing – original draft. **Joel A. McQuaid:** Formal analysis, Methodology, Software, Supervision, Writing – review & editing. **Christoph Brehm:** Conceptualization, Funding acquisition, Supervision, Writing – review & editing. **Alexandre Martin:** Conceptualization, Funding acquisition, Supervision, Writing – review & editing.

Declaration of competing interest

The authors declare that they have no known competing financial interests or personal relationships that could have appeared to influence the work reported in this paper.

Data availability

Data will be made available on request.

Acknowledgements

The authors would like to recognize and show appreciation for the financial support provided by NASA Kentucky EPSCoR RA Award no. 80NSSC19M0144 (E. Stern technical monitor) and NASA EPSCoR R3 Award no. 80NSSC19M0084 (M. Barnhardt technical monitor). Christoph Brehm and Joel McQuaid would also like to recognize and show appreciation for the financial support provided by National Science Foundation under award CBET-2146100 with Dr. R. Joslin as Program Manager. The authors would also like to thank Justin Haskins and Georgios Chatzigeorgis from NASA Ames Research Center for providing valuable data for camphor properties. The authors would also like to thank the University of Kentucky Center for Computational Sciences and Information Technology Services Research Computing for their support and use of the Lipscomb Compute Cluster and associated research computing resources. In addition, the authors highly appreciate the valuable discussions with Daniele Bianchi, Alessandro Turchi, and Marco Rotondi from Sapienza University of Rome and VKI.

Appendix A

The following table presents the species' characteristic vibrational temperatures used to model the vibrational activation of both air species. Camphor was assumed to not be vibrationally activated in this work due to the low temperature of the fluid.

Table 5 provides the coefficients for the Blottner curve fit for air species viscosity.

Table 6 provides the input to the Mutation++ library of the camphor thermodynamic properties in NASA 7 format. The coefficients for the

Table 4
Air species characteristic vibrational temperature.

Species	θ_v (K)
N_2	3395.0
O_2	2239.0

Table 5
Blottner curve fit coefficients for air species.

Species	A_s	B_s	C_s
N_2	2.68142×10^{-2}	3.177838×10^{-1}	$-1.13155513 \times 10^{1}$
O_2	4.49290×10^{-2}	-8.261580×10^{-2}	$-9.20194750 \times 10^{0}$

Table 6
Thermodynamic data coefficients for camphor in NASA-7 format.

```
 C10H16O          a03/21C 10.H 16.O  1.   0.G   200.000  550.0000     152.2300 1
8.32598410E+00-1.13808460E-02 3.43046471E-04-5.53445260E-07 2.87556562E-10     2
-3.62060071E+04-7.19365555E+00 8.32598410E+00-1.13808460E-02 3.43046471E-04    3
-5.53445260E-07 2.87556562E-10-3.62060071E+04-7.19365555E+00 0.00000000E+00    4
```

Table 7
Input to collision table in Mutation++ library for camphor species. The data was obtained from QC simulation by Haskins [40].

```
<dipole-polarizabilities units="{\AA}-{\AA}-{\AA}">
    <species name="C16H10O"      value=" 16.5336"/>
</dipole-polarizabilities>

<effective-electrons>
    <species name=" C16H10O"      value=" 17.046"/>
</effective-electrons>
```

Table 8
Camphor viscosity and thermal conductivity curve fit coefficients [37,38,40].

Coefficient	Yaws		Haskins	
	μ	κ	μ	κ
c_0	-7.4390×10^{-8}	-4.3828×10^{-3}	1.5210×10^{-6}	-8.4400×10^{-3}
c_1	2.0215×10^{-8}	1.0500×10^{-5}	3.0470×10^{-8}	6.6000×10^{-5}
c_2	1.2145×10^{-12}	1.3260×10^{-7}	0.0000	6.8800×10^{-8}
c_3	-1.5620×10^{-15}	-4.9499×10^{-11}	0.0000	2.6600×10^{-11}

NASA 7 polynomials were generated based on the data obtained from quantum chemical simulation by Haskins [40].

Table 7 provides the input to the Mutation++ library of the camphor collision integral data, obtained from quantum chemical simulation.

Camphor viscosity and thermal conductivity were modeled with two separate models from Yaws [37,38] and Haskins [40], each with a set of polynomial coefficients which are given in Table 8. The Yaws viscosity model is valid for the range of 200 K $\leq T \leq$ 1500 K whereas the Haskins model is valid for the range of 200 K $\leq T \leq$ 800 K. Camphor diffusivity was modeled with two separate models from [39] and Haskins [40]. The Yaws' model is provided in polynomial curve fit form in Eqn. (18) and the coefficients are provided in Table 9.

In the second model, the diffusion coefficient of camphor was computed with the Mutation++ library based on the thermodynamic and collision integral data obtained in quantum chemical simulation. The temperature and pressure-dependent data of the diffusion coefficient was curve fitted with a polynomial, provided in Eqn. (19), where the coefficients are provided in Table 10.

Table 9
Coefficients for camphor in air diffusion coefficient for 200 K $\leq T \leq$ 1000 K from Yaws [39].

Coefficient	c_0	c_1	c_2
Value	-3.6210×10^{-6}	1.96310×10^{-8}	4.46030×10^{-11}

Table 11 gives the coefficients for camphor vapor pressure defined in Eqn. (35).

Table 12 gives the properties of solid camphor and copper.

Table 10
Coefficients for camphor diffusion coefficient in air for 200 K $\leq T \leq$ 800 K and 1000 Pa $\leq p \leq$ 70,000 Pa from Haskins [40].

Coefficient	Value
B_1	0.000018912588145
B_2	0.003222763711371
B_3	-0.429233442816354
B_4	0.408695307746624
B_5	-1.000951241396257

Table 11
Camphor vapor pressure coefficients for exponential form. Fitted from the logarithmic form in Ref. [32].

	Coefficients
A	120170
B	-6117.1
C	12.654

Table 12
Solid camphor [45,53] and copper properties.

Parameter	Camphor	Copper
ρ_s (kg/m^3)	990	8890
k_s (W/m-K)	0.2	388
$c_{p,s}$ (J/kg-K)	1781	385
h_s^f (MJ/kg)	-2.1	0
ϵ	0.88	-

References

[1] D. Callaway, M. Reeder, R. Greendyke, Experimental studies of low temperature ablation using dry ice, in: 15th AIAA International Space Planes and Hypersonic Systems and Technologies Conference, 2008, https://doi.org/10.2514/6.2008-2554.

[2] R. Baker, Low temperature ablator nosetip shape change at angle of attack, in: 10th Aerospace Sciences Meeting, 1972, https://doi.org/10.2514/6.1972-90.

[3] D. Bianchi, A. Turchi, Numerical analysis on the sublimation of low-temperature ablator models undergoing shape change in a supersonic wind-tunnel, https://doi.org/10.13009/EUCASS2019-800, 2019.

[4] A.F. Charwat, Exploratory studies on the sublimation of slender camphor and naphthalene models in a supersonic wind-tunnel, Research Memoranda RM-5506-ARPA Rand Corporation, Santa Monica, CA, 1968, https://www.rand.org/pubs/research_memoranda/RM5506.html.

[5] H.W. Stock, Surface patterns on subliming and liquefying ablation materials, AIAA J. 13 (9) (1975) 1217–1223, https://doi.org/10.2514/3.6973.

[6] F. Lipfert, J. Genovese, An experimental study of the boundary layers on low-temperature subliming ablators, AIAA J. 9 (7) (1971) 1330–1337, https://doi.org/10.2514/3.49943.

[7] R.J. Swigart, Cross-hatching studies-a critical review, AIAA J. 12 (10) (1974) 1301–1318, https://doi.org/10.2514/3.49482.

[8] L. Trevino, G.V. Candler, Numerical simulation of regular surface patterns on subliming ablative materials, in: 53rd AIAA Aerospace Sciences Meeting, 2015, https://doi.org/10.2514/6.2015-1452.

[9] S.D. Dungan, J.A. McQuaid, A.L. Zibitsker, A. Martin, C. Brehm, Numerical investigation of fluid-ablation interactions for a Mach 5.3 transitional boundary layer flow over a 13 degree cone, in: AIAA SCITECH 2023 Forum, 2023, 0476, https://doi.org/10.2514/6.2023-0476.

[10] M. Rotondi, M.T. Migliorino, D. Bianchi, P. Pagani, A. Turchi, Numerical assessment of camphor ablation flight relevance in hypersonic wind-tunnel testing, J. Spacecr. Rockets (2022) 1–18, https://doi.org/10.2514/1.A35318.

[11] Y.-K. Chen, F.S. Milos, Ablation and thermal response program for spacecraft heatshield analysis, J. Spacecr. Rockets 36 (3) (1999) 475–483, https://doi.org/10.2514/2.3469.

[12] C.B. Moyer, R.A. Rindal, An analysis of the coupled chemically reacting boundary layer and charring ablator. Part 2-finite difference solution for the in-depth response of charring materials considering surface chemical and energy balances, Contractor Report NASA-CR-1061, NASA, 1968, https://ntrs.nasa.gov/citations/19680017220.

[13] M. Stackpoole, S. Sepka, I. Cozmuta, D. Kontinos, Post-flight evaluation of stardust sample return capsule forebody heatshield material, in: 46th AIAA Aerospace Sciences Meeting and Exhibit, 2008, https://doi.org/10.2514/6.2008-1202.

[14] M. Mahzari, R.D. Braun, T.R. White, D. Bose, Inverse estimation of the Mars science laboratory entry aeroheating and heatshield response, J. Spacecr. Rockets 52 (4) (2015) 1203–1216, https://doi.org/10.2514/1.A33053.

[15] F.S. Milos, Y.-K. Chen, Ablation and thermal response property model validation for phenolic impregnated carbon ablator, J. Spacecr. Rockets 47 (5) (2010) 786–805, https://doi.org/10.2514/1.42949.

[16] B. Blackwell, R. Hogan, One-dimensional ablation using Landau transformation and finite control volume procedure, J. Thermophys. Heat Transf. 8 (2) (1994) 282–287, https://doi.org/10.2514/3.535.

[17] A.J. Amar, B.F. Blackwell, J.R. Edwards, One-dimensional ablation using a full Newton's method and finite control volume procedure, J. Thermophys. Heat Transf. 22 (1) (2008) 71–82, https://doi.org/10.2514/1.29610.

[18] A. Martin, I.D. Boyd, Non-Darcian behavior of pyrolysis gas in a thermal protection system, J. Thermophys. Heat Transf. 24 (1) (2010) 60–68, https://doi.org/10.2514/1.44103.

[19] A. Martin, I.D. Boyd, Strongly coupled computation of material response and nonequilibrium flow for hypersonic ablation, J. Spacecr. Rockets 52 (1) (2015) 89–104, https://doi.org/10.2514/1.A32847.

[20] P. Schrooyen, K. Hillewaert, T.E. Magin, P. Chatelain, Fully implicit discontinuous Galerkin solver to study surface and volume ablation competition in atmospheric entry flows, Int. J. Heat Mass Transf. 103 (2016) 108–124, https://doi.org/10.1016/j.ijheatmasstransfer.2016.07.022.

[21] U. Duzel, A. Martin, Modeling high velocity flow through porous media, in: AIAA Scitech 2020 Forum, 2020, https://doi.org/10.2514/6.2020-0486.

[22] H. Zhang, H. Weng, A. Martin, Simulation of flow-tube oxidation on the carbon preform of PICA, in: 52nd Aerospace Sciences Meeting, 2014, https://doi.org/10.2514/6.2014-1209.

[23] Y.-K. Chen, T. Gökçen, Implicit coupling approach for simulation of charring carbon ablators, J. Spacecr. Rockets 51 (3) (2014) 779–788, https://doi.org/10.2514/1.A32753.

[24] D.W. Kuntz, B. Hassan, D.L. Potter, Predictions of ablating hypersonic vehicles using an iterative coupled fluid/thermal approach, J. Thermophys. Heat Transf. 15 (2) (2001) 129–139, https://doi.org/10.2514/2.6594.

[25] P. Schrooyen, A. Turchi, K. Hillewaert, P. Chatelain, T.E. Magin, Two-way coupled simulations of stagnation-point ablation with transient material response, Int. J. Therm. Sci. 134 (2018) 639–652, https://doi.org/10.1016/j.ijthermalsci.2018.08.014.

[26] J. McQuaid, A. Zibitsker, A. Martin, C. Brehm, Heat flux predictions for high speed flows with an immersed boundary method, in: AIAA Aviation Forum, American Institute of Aeronautics and Astronautics, 2021, https://doi.org/10.2514/6.2021-3145.

[27] J.A. McQuaid, A.L. Zibitsker, A. Martin, C. Brehm, Simulation of graphite ablation using an overset near body solver on an adaptive block-structured cartesian off-body grid, in: AIAA Aviation 2022 Forum, 2022, https://doi.org/10.2514/6.2022-4088, AIAA Paper 2022–4088.

[28] A.L. Zibitsker, J. McQuaid, C. Brehm, A. Martin, Fully-coupled simulation of low temperature ablator and hypersonic flow solver, in: AIAA SciTech 2022 Forum, 2022, https://doi.org/10.2514/6.2022-0676.

[29] A.L. Zibitsker, J.A. McQuaid, C. Brehm, A. Martin, Study of a two-dimensional shape change of blunt-body geometries at hypersonic conditions using fully coupled simulation, in: AIAA AVIATION 2022 Forum, 2022, https://doi.org/10.2514/6.2022-4006.

[30] J.A. McQuaid, A.L. Zibitsker, A. Martin, C. Brehm, Heat flux predictions using a 3D near body solver on an adaptive block-structured Cartesian off-body grid, in: AIAA Science and Technology Forum and Exposition Forum 2023, 2023, https://doi.org/10.2514/6.2023-1799, AIAA Paper 2023–1799.

[31] A. Turchi, S. Paris, W. Agostinelli, F. Grigat, S. Löhle, D. Bianchi, L. Ferracina, Assessment of the effect of heat-shield ablation on the aerodynamic performance of re-entry capsules in hypersonic flows, in: 8th European Conference for Aeronautics and Aerospace Sciences, 2019, https://www.eucass.eu/component/docindexer/?task=download&id=5705.

[32] D. Bianchi, M.T. Migliorino, M. Rotondi, A. Turchi, Numerical analysis and wind tunnel validation of low-temperature ablators undergoing shape change, Int. J. Heat Mass Transf. 177 (2021) 121430, https://doi.org/10.1016/j.ijheatmasstransfer.2021.121430.

[33] C.-M. Hung, Definition of contravariant velocity components, in: 3rd Theoretical Fluid Mechanics Meeting, 2002, p. 3202, https://doi.org/10.2514/6.2002-3202.

[34] K. Sutton, P.A. Gnoffo, Multi-component diffusion with application to computational aerothermodynamics, in: 7th AIAA/ASME Joint Thermophysics and Heat Transfer Conference, AIAA, 1998, https://doi.org/10.2514/6.1998-2575.

[35] F.G. Blottner, M. Johnson, M. Ellis, Chemically Reacting Viscous Flow Program for Multi-Component Gas Mixtures, Tech. Rep. SC-RR-70-754, Sandia Laboratories, January 1971, https://doi.org/10.2172/4658539.

[36] W.G. Vincenti, C.H. Kruger, Introduction to Physical Gas Dynamics, 1st ed., Krieger Pub Co, New York, NY, 1975, https://doi.org/10.1017/S0001924000057304.
[37] C.L. Yaws, P. Bahadur, Viscosity of gas–organic compounds, in: Transport Properties of Chemicals and Hydrocarbons, Elsevier, 2009, pp. 1–92.
[38] C.L. Yaws, Thermal conductivity of gas–organic compounds, in: Transport Properties of Chemicals and Hydrocarbons, Elsevier, 2009, pp. 201–291.
[39] C.L. Yaws, Diffusion coefficient in air - organic compounds, in: Transport Properties of Chemicals and Hydrocarbons, Elsevier, 2009, pp. 201–291.
[40] J. Haskins, Private communication, 2021.
[41] J.B. Scoggins, T.E. Magin, Development of mutation++: multicomponent thermodynamic and transport properties for ionized plasmas written in c++, in: 11th AIAA/ASME Joint Thermophysics and Heat Transfer Conference, 2014, https://doi.org/10.2514/6.2014-2966.
[42] B.J. McBride, M.J. Zehe, S. Gordon, NASA Glenn coefficients for calculating thermodynamic properties of individual species, Tech. Rep. NASA/TP-2002-211556, National Aeronautics and Space Administration, John H. Glenn Research Center, 2002.
[43] C. Brehm, On consistent boundary closures for compact finite-difference WENO schemes, J. Comput. Phys. 334 (2017) 573–581, https://doi.org/10.1016/j.jcp.2016.12.057.
[44] L.H. Thomas, Elliptic Problems in Linear Difference Equations over a Network, Watson Sci. Comput. Lab. Rept., vol. 1, Columbia University, New York, 1949, p. 71.
[45] T.K. Sherwood, C. Johannes, The maximum rate of sublimation of solids, AIChE J. 8 (5) (1962) 590–593, https://doi.org/10.1002/aic.690080505.
[46] L. Anderson, E. Bartlett, R. Kendall, W. Nicolet, Further studies of the coupled chemically reacting boundary layer and charring ablator. Part 1 - Summary final report, Tech. Rep. NASA-CR-92471, NASA, 1968.
[47] E. Bartlett, R. Kendall, An analysis of the coupled chemically reacting boundary layer and charring ablator. Part 3 - Nonsimilar solution of the multicomponent laminar boundary layer by an integral matrix method, Tech. Rep. NASA-CR-1062, NASA, 1968.
[48] A. Turchi, Private communication, 2021.
[49] G.E. Palmer, M.J. Wright, Comparison of methods to compute high-temperature gas viscosity, J. Thermophys. Heat Transf. 17 (2) (2003) 232–239, https://doi.org/10.2514/2.6756.
[50] G. Bellas Chatzigeorgis, J.B. Haskins, J.B. Scoggins, Transport properties for neutral C, H, N, O, and Si-containing species and mixtures from the Gordon and McBride thermodynamic database, Phys. Fluids 34 (8) (2022), https://doi.org/10.1063/5.0098060.
[51] A.L. Zibitsker, J. McQuaid, C. Brehm, A. Martin, Deviation from equilibrium thermochemistry and aerodynamic heating assumptions in the ablation process of camphor, in: AIAA Aviation 2023 Forum, 2023, https://doi.org/10.2514/6.2023-3486.
[52] A. Valli, G. Carey, A. Coutinho, Control strategies for timestep selection in finite element simulation of incompressible flows and coupled reaction–convection–diffusion processes, Int. J. Numer. Methods Fluids 47 (3) (2005) 201–231, https://doi.org/10.1002/fld.805.
[53] C.L. Yaws, C. Gabbula, Yaws, in: Handbook of Thermodynamic and Physical Properties of Chemical Compounds, Knovel, 2003.